Dalton
Transactions

An international journal of inorganic chemistry

rsc.li/dalton

Lysosome - targeting

ROYAL SOCIETY
OF CHEMISTRY
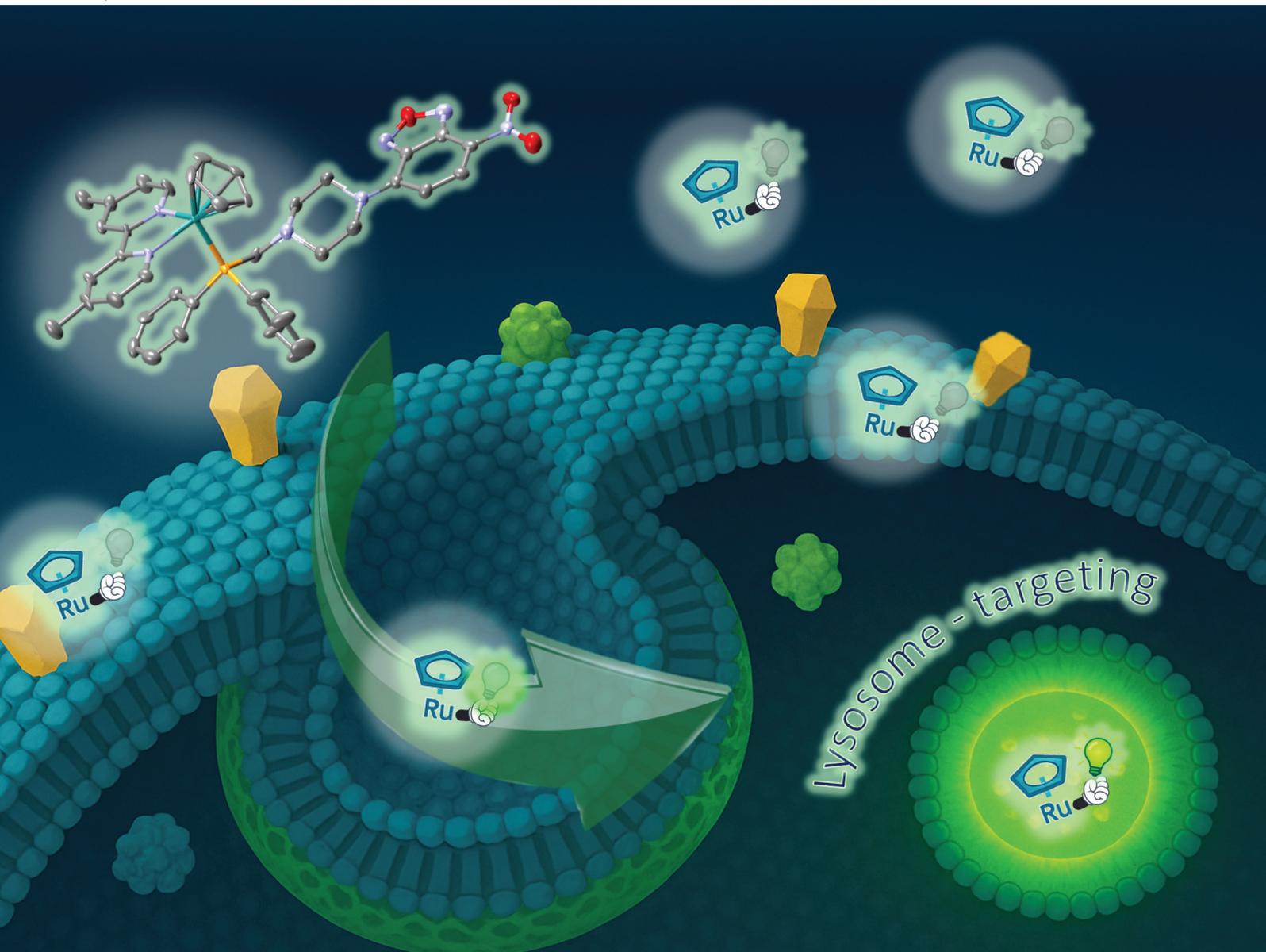
PAPER
Lígia C. Gomes-da-Silva, Andreia Valente *et al.*
Lysosome-targeted Ru(ɪɪ)–cyclopentadienyl organometallic
anticancer complexes

Lysosome-targeted Ru(II)–cyclopentadienyl organometallic anticancer complexes

Ricardo G. Teixeira, †[a] Lívia Stenico,[b] Xavier Fontrodona,[c] Isabel Romero,[c] Radosław Starosta,[a,d] Maria João Moreno,[b,e] Ana Isabel Tomaz,[a] Lígia C. Gomes-da-Silva*[b,e] and Andreia Valente *[a]

Cancer continues to pose a significant global health burden, prompting ongoing exploration of innovative therapeutic strategies. Ruthenium-based complexes have emerged as promising alternatives to platinum drugs due to their generally favorable pharmacological profiles. In this work, we report the synthesis and characterization of a novel series of fluorescent Ru(II)–cyclopentadienyl organometallic complexes of general formula $[Ru(\eta^5-C_5H_5)(NN)(Ph_2P-CH_2-pip-NBD)][PF_6]$ (**1–5**), where NN represents a bipyridine or phenanthroline-based ligand and $Ph_2P-CH_2-pip-NBD$ is a 4-nitrobenzo-2-oxa-1,3-diazole (NBD)-derived fluorescent phosphane conjugate. Structural characterization confirmed their piano-stool geometry *via* NMR, FTIR, UV-Vis, fluorescence spectroscopy, and X-ray crystallography (for **1**, **3** and **5**). The complexes exhibit notable stability in both organic and aqueous media. Cytotoxicity screening across three cancer cell lines (4T1 murine epithelial breast cancer, CT26 murine colon carcinoma, U2OS human osteosarcoma) and one non-cancerous line (3T3 murine embryonic fibroblasts) revealed that complexes **1**, **3**, and **5** display potent anticancer activity, particularly against U2OS. Fluorescence-based uptake and confocal microscopy demonstrated efficient internalization, primarily through caveolin-mediated endocytosis, and preferential accumulation in lysosomes. Enhanced fluorescence in acidic environments and co-localization with lysosomal markers confirm lysosomal tropism, highlighting the dual role of the NBD fluorophore for traceability and subcellular targeting. Additional mechanistic studies revealed that complexes **1**, **3**, and **5** induce oxidative stress and trigger apoptosis, suggesting that ROS generation contributes to their cytotoxic activity. These findings establish this class of compounds as promising lysosome-targeting agents.

Introduction

Cancer is a global health problem with an enormous worldwide impact, with more than 19 million new cases and nearly 10 million deaths worldwide in 2022.[1] Statistics from the World Health Organization (WHO) indicate that these numbers are estimated to increase by almost 60% in the next two decades.[2] Over the last few decades, many examples of compounds involving transition metal ions emerged as efficient anticancer agents due to their variable oxidation states, superior stability, and selectivity towards cancer cells.[3,4] Cisplatin was the first anticancer metallodrug approved by the Food and Drug Administration (FDA) and is used to treat testicular and ovarian cancer.[5] Besides cisplatin, carboplatin and oxaliplatin have also been used to treat cancer worldwide, despite limitations such as poor aqueous solubility, low selectivity, drug resistance, and high *in vivo* toxicity that hamper their therapeutic capacity.[6]

Over time, ruthenium complexes have consistently shown encouraging results as the next prominent class of metal-based anticancer therapeutics.[7] Until now, special interest in the preparation of ruthenium-based compounds has been supported by their excellent antitumor properties and good pharmacological profile both *in vitro* and *in vivo*,[8–11] including their cytotoxicity in platinum-resistant cells[12] and ability to

[a] Centro de Química Estrutural, Institute of Molecular Sciences, Departamento de Química e Bioquímica, Faculdade de Ciências, Universidade de Lisboa, Campo Grande, 1749-016 Lisboa, Portugal. E-mail: amvalente@ciencias.ulisboa.pt, ligia.silva@uc.pt

[b] Coimbra Chemistry Center – Institute of Molecular Sciences (CQC-IMS), University of Coimbra, 3004-535 Coimbra, Portugal

[c] Departament de Química and Serveis Tècnics de Recerca, Universitat de Girona, C/M. Aurèlia Campmany, 69, E-17003 Girona, Spain

[d] Faculty of Chemistry, University of Wrocław, F. Joliot-Curie 14, 50-383 Wrocław, Poland

[e] Department of Chemistry, University of Coimbra, 3004-535 Coimbra, Portugal

† Current address: Centro de Química Estrutural, Institute of Molecular Sciences, Instituto Superior Técnico, Universidade de Lisboa, Av. Rovisco Pais 1, 1049–001 Lisboa, Portugal; and Associação do Instituto Superior Técnico *para* a Investigação e Desenvolvimento (IST-ID), Avenida António José de Almeida 12, 1000-043 Lisboa Portugal.

reduce the formation of metastasis.[13,14] However, and despite their promising anticancer properties, only three Ru(III) compounds (namely NAMI-A[14] ([ImH][*trans*-Ru(Cl)$_4$(Im)(DMSO)]; Im = imidazole and DMSO = dimethylsulfoxide), KP1019[15] and its soluble salt NKP1339[16] (KP1019 = [IndH][*trans*-RuCl$_4$(Ind)$_2$], Ind = indazole; NKP1339 = [Na][*trans*-RuCl$_4$(Ind)$_2$])), together with a Ru(II) photosensitizer compound (TLD1433, [Ru (Me$_2$bipy)$_2$(IP-3T)][Cl]$_2$ (Me$_2$bipy = 4,4′-dimethyl-2,2′-bipyridine; IP = imidazo[4,5 *f*][1,10]phenanthroline; 3T = α-terthienyl[17])) have entered clinical trials.

Other classes of ruthenium anticancer agents, mostly based on the ruthenium–arene motif, have been developed. The Ru (II) arene scaffold has proven to be a very useful structure for the development of anticancer drugs due to its stability, solubility, and lipophilicity.[18] Ru(II) arene complexes have an octahedral geometry, in which the arene ligand occupies three coordination positions and other ligands can bind to the three remaining coordination sites, giving a three-legged piano-stool type of structure. The combination of the ruthenium ion with arene ligands confers more hydrophobic character to the metal-based scaffold, promoting passive diffusion across the cell membrane and enhancing their cellular accumulation.[19] In addition, the nature of the arene ligands assists in the cell uptake and the interaction with potential targets.[20]

In this frame, our research group has developed a library of organometallic compounds by exploring the chemistry of the ruthenium-(η^5-cyclopentadienyl) ('RuCp') scaffold within the therapeutic context. We have focused on the general structure [Ru(Cp)(NN)(P)]$^+$ (Cp = η^5-cyclopentadienyl or Cp-derivatized; NN = *N,N*-heteroaromatic bidentate ligand (*e.g.*, 2,2′-bipiridine or its derivatives); P = triphenylphosphane or its derivatives), which has shown remarkable anticancer activity against several human cancer cell lines, especially against resistant and more aggressive cancer cells.[21] Yet, up to now, we have not explored the incorporation of a fluorescent label for traceability purposes. In this context, the 4-nitrobenzo-2-oxa-1,3-diazole (NBD) fluorophore emerges as a promising candidate, as it has already been employed in the derivatization of various therapeutic agents, including platinum-based complexes,[22,23] as well as other small molecules. These studies demonstrate that NBD can be used to monitor cellular uptake, efflux, and intracellular distribution without significantly altering the biological activity of the parent compound. Notably, some of us have previously reported the synthesis of a phosphane derivative, 7-nitro-4-(4-(diphenylphosphinomethyl)piperazin-1-yl)-2,1,3-benzoxadiazole (Ph$_2$P-CH$_2$-pip-NBD), which has shown potential as a molecular probe for imaging living cells.[24] This compound could conveniently replace triphenylphosphane in our complexes as exemplified by Florindo *et al.*, who described half-sandwich 'RuCp' complexes bearing NBD-derived 2-pyridine and phosphane ligands with antimalarial activity.[25] Beyond enabling traceability, this substitution facilitates lysosome targeting due to the preferential accumulation of such probes in acidic organelles. Moreover, targeting the endosomal/lysosomal pathway has emerged as a key target in cancer treatment strategies by promoting lysosomal membrane permeabilization, disrupting autophagy, and exploiting the acidic environment to enhance drug activation.[26] Lysosomes contain a variety of hydrolases capable of degrading both intra- and extracellular components. Upon release into the cytosol, these enzymes can contribute to the breakdown of apoptotic proteins, ultimately triggering the mitochondrial apoptotic pathway and/or other cell death modalities.[27] Such a mechanism of action has been observed for certain lysosome-targeting Ru(III) coordination compounds,[28] as well as for some half-sandwich Ru(II)(η^6-arene) complexes,[29–33] with confocal microscopy playing a key role in confirming organelle-specific localization. However, no such reports exist for half-sandwich Ru(II)(η^5-Cp) complexes, likely due to the absence of suitable conjugate structures – and thus the lack of intrinsic fluorescence – required for effective imaging.

In this study, we present the synthesis of a novel family of fluorescent 'RuCp' organometallic complexes with the general formula [Ru(η^5-C$_5$H$_5$)(NN)(Ph$_2$P-CH$_2$-pip-NBD)][PF$_6$] (**1–5**, Fig. 1) where Ph$_2$P-CH$_2$-pip-NBD is 7-nitro-4-(4-(diphenylphosphinomethyl-piperazin-1-yl)-2,1,3-benzoxadiazole) and NN represents a N,N-donor (bipyridine or phenanthroline). Ligands of type 4,4′-R-2,2′-bipyridine (R = CH$_3$, OCH$_3$, CH$_2$OH, CH$_2$Biotin) were selected for this study as an extension of our previous work, which indicated the possible role of some of them in surmounting multidrug resistance (MDR).[34–37]

Results and discussion

Synthesis and characterization

Reaction of [Ru(η^5-C$_5$H$_5$)(NCCH$_3$)$_3$][PF$_6$] with 1 mol equivalent of the corresponding *N,N*-heteroaromatic bidentate and 1 mol equivalent of Ph$_2$P-CH$_2$-pip-NBD afforded the complexes [Ru (η^5-C$_5$H$_5$)(NN)(Ph$_2$P-CH$_2$-pip-NBD)][PF$_6$] (**1–5**, where Ph$_2$P-CH$_2$-pip-NBD = 7-nitro-4-(4-(diphenylphosphinomethyl-piperazin-1-yl)-2,1,3-benzoxadiazole) and NN = 4,4′-dimethyl-2,2′-bipridine (**1**); 4,4′-bis(hydroxymethyl)-2,2′-bipyridine (**2**); 4,4′-dimethoxy-2,2′-bipyridine (**3**); 2,2′-bipy-4,4′-dibiotin ester (**4**); 1,10-phenanthroline (**5**)) in very good yields (Scheme S1 of the SI). Complex **4** was first prepared *via* direct reaction with 2,2′-bipy-4,4′-dibiotin ester. However, this strategy proved unsuccessful, and we were only able to detect small amounts of **4** using this route. Based on our previous work applying the "chemistry-on-the-complex" concept to organometallic complexes,[36,37] we then proceeded with the direct conjugation reaction of biotin, using complex **2** as a platform, *N*-(3-dimethylaminopropyl)-*N*′-ethylcarbodiimide hydrochloride as coupling agent, and DMAP as the catalyst (Scheme S1 of the SI). The complexes were isolated as dark red crystalline solids and were characterized by FTIR, UV-Vis, fluorescence, and NMR spectroscopies. Elemental analysis and electron spray ionization mass spectrometry (ESI-MS) supported the proposed formulation for all compounds. In addition, single-crystal X-ray diffraction studies were possible for compounds **1, 3** and **5**, which corroborate the proposed structures.
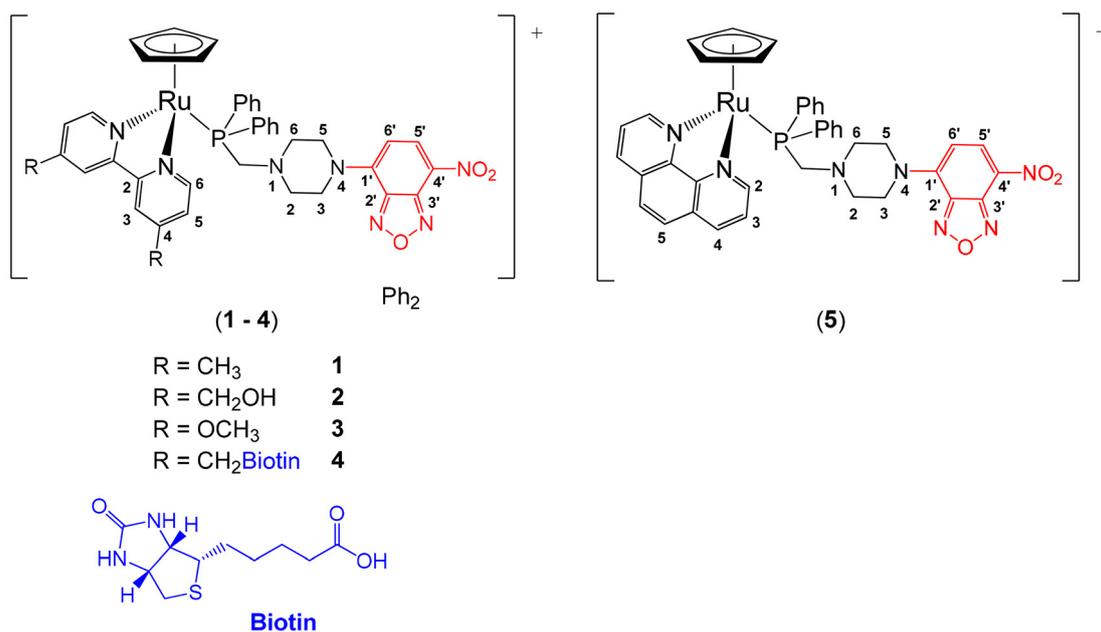
Fig. 1 Chemical structures of compounds **1–5**, including the numbering scheme for spectral assignments. All complexes were isolated as hexafluorophosphate salts.

Solid state infrared spectra (KBr pellets) of the new complexes presented the characteristic stretching bands of the cyclopentadienyl (νC–H ~3050 cm^{-1}) and the phenyl aromatic rings (νC–H and νC=C at ~3050–3100 cm^{-1} and ~1430 cm^{-1}, respectively) and the typical vibrational bands for PF$_6^-$ anion (stretching νPF$_6$ at 843 cm^{-1} and symmetric bending δPF$_6$ at 558 cm^{-1}, respectively). The successful introduction of the bidentate diimines and Ph$_2$P-CH$_2$-pip-NBD ligands into the coordination sphere of the metal was confirmed by the complete disappearance of the stretching band of the acetonitrile ligands (νC≡N ~2280 cm^{-1}) present at the starting material [Ru(η^5-C$_5$H$_5$)(NCCH$_3$)$_3$][PF$_6$] and is fully supported by NMR data as well (Fig. S1–S15 of the SI). The overall analysis of the ^{1}H and ^{31}P{^{1}H} NMR spectra of complexes **1–5** indicate the displacement of the three acetonitrile ligands in [Ru(η^5-C$_5$H$_5$)(NCCH$_3$)$_3$]$^+$ by the chosen N,N-heteroaromatic and phosphane co-ligands. In all cases, the resonances expected for the cyclopentadienyl, alkyl diphenylphosphane, and bipyridine/phenanthroline protons are observed in a 1 : 1 : 1 ratio, confirming the stoichiometry of the ligands in the final complex. The assignment of all resonances observed in ^{1}H,^{13}C{^{1}H}-APT NMR (atom numbering is shown in Fig. 1) was supported by analysis of 2D NMR experiments (^{1}H–^{1}H COSY, ^{1}H–^{13}C HMQC and HMBC).

In short, the ^{1}H NMR spectra of complexes **1–5** show discrete resonances attributed to the cyclopentadienyl ring in the typical range for cationic 'RuCp' compounds (~δ 5.00–5.30 ppm in acetone-d_6). Upon coordination of the N,N-bidentate, all the aromatic protons show a significant deshielding, especially the protons next to the coordinated nitrogen ($\Delta\delta \approx 0.7$ ppm), and a shielding on the H3 protons of the 2,2′-bipyridine derivative (ΔH3 $\approx$ −0.5 ppm). This proves the successful σ-coordination of the diimine ligand to the ruthenium center.$^{34–37}$ The ^{31}P{^{1}H} NMR spectrum of complexes **1–5** is characterized by the presence of a sharp resonance at δ ~45 ppm (acetone-d_6), which is a significant deshielding of the phosphorous nuclei resonance is observed ($\Delta\delta$ up to 72 ppm), indicating the successful coordination of the alkyl-diphenylphosphane to the metal center. Detailed ^{13}C{^{1}H}-APT NMR data are described in the experimental section and follow the effects discussed with the ^{1}H NMR results.

Complexes **1–5** are soluble in organic solvents such as dichloromethane, methanol, acetone, acetonitrile, and dimethylsulfoxide, and insoluble in water, n-hexane, and diethyl ether. The optical absorption and emission spectra of all compounds were recorded using up to 10^{-3} to 10^{-6} M solutions in acetonitrile and dimethylsulfoxide at room temperature. Fig. S16 (SI) shows the electronic absorption spectra recorded in acetonitrile for complex **1** as a representative example. All complexes showed absorption bands in the UV region (λ = 200–325 nm) that are ascribed to electronic transitions occurring in the organometallic fragment ({[Ru(η^5-C$_5$H$_5$)(Ph$_2$P-CH$_2$-pip-NBD)]$^+$}) and the coordinated N,N-ligand. In addition to these bands, this series of organometallics shows a common feature related to the presence of the fluorophore in their structure: the usual metal-to-ligand charge transfer (MLCT) band, frequently observed for this type of organometallic complexes (at λ ~450 nm), is masked by the absorption of the NBD-derived probe. The fluorescent unit on the organometallic structure, which aims to probe the cellular uptake and distribution of the compounds, was further studied by fluorescence spectroscopy. The luminescence quantum yields (Table S1 of the SI) of the

Ph$_2$P-CH$_2$-pip-NBD coordinated complexes (Φ_F **1**: 0.3%, **2**: 0.1%, **3**: 0.2%, **4**: 0.2%, **5**: 0.2%) were found to be significantly lower than that of the Ph$_2$P-CH$_2$-pip-NBD free ligand (ΦF: 1.0%). Fig. S17 (SI) shows the absorption and emission spectra of all (non-protonated) complexes in dimethylsulfoxide.
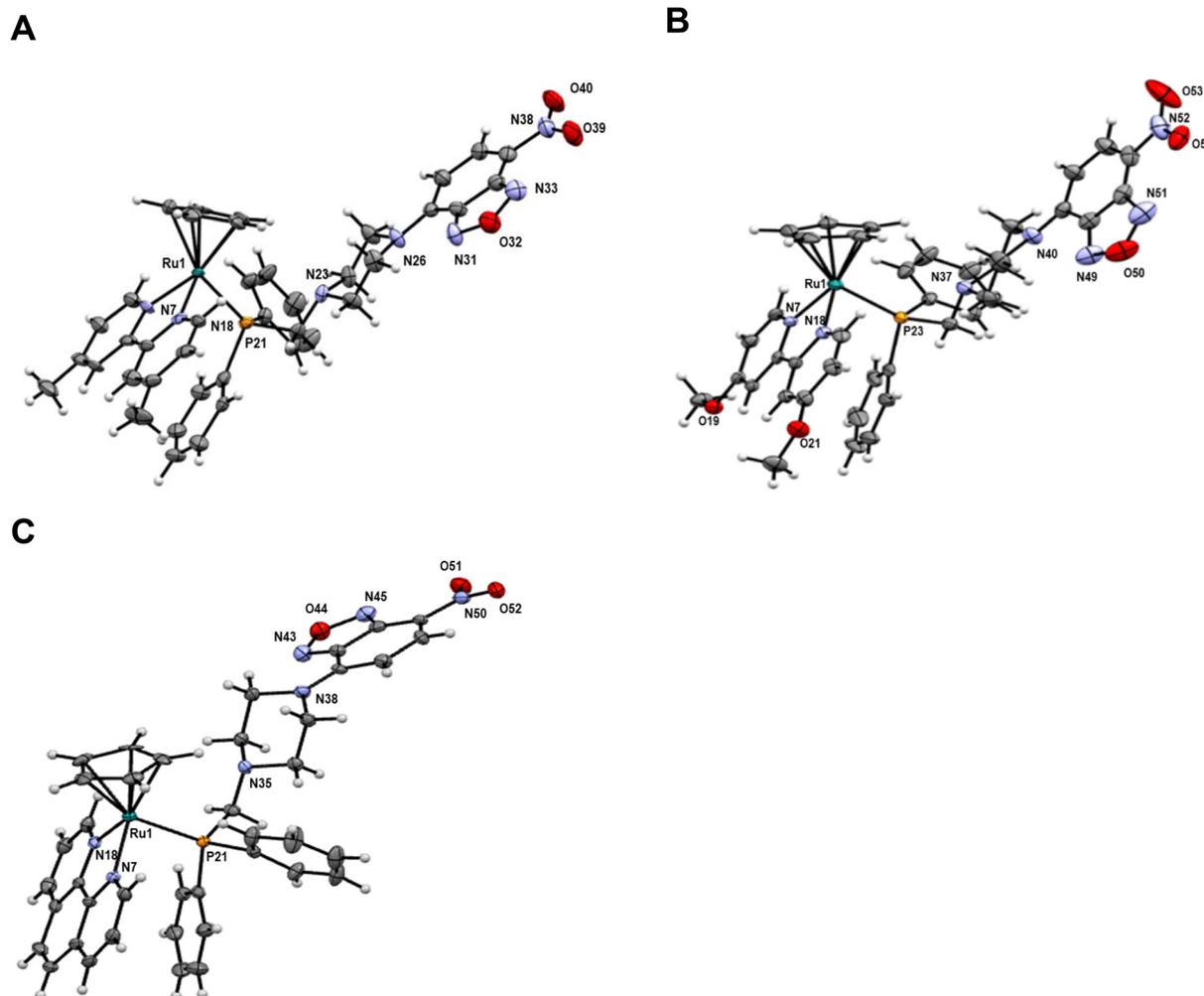
X-ray crystallography

The crystal structures of compounds **1**, **3**, and **5** were confirmed by single-crystal X-ray diffraction analysis. ORTEP diagrams of their molecular structures are shown in Fig. 2, and the main crystallographic data are described in the Experimental section. Selected lengths and angles are presented in Table 1.

1 and **3** crystallize in the triclinic system (centrosymmetric space group $P\bar{1}$) whereas **5** crystallize in the monoclinic system (space group $P1\ 21/c1$). All the compounds displayed racemic crystals, with the presence of the two enantiomers. Each asymmetric unit includes a cationic organometallic 'RuCp' complex and a hexafluorophosphate anion. The asymmetric unit for **1** contains one acetone molecule. All complexes feature a six-

coordinate Ru(II) center with a pseudo-octahedral piano-stool geometry. The ruthenium ion is coordinated by an η^5-cyclopentadienyl ring in a π-bonded fashion, one disubstituted bipyridyl ligand (**1**, –CH$_3$; and **3**, –OCH$_3$) or a phenanthroline ligand (**5**), and the remaining coordination site is occupied by the phosphine ligand Ph$_2$P-CH$_2$-pip-NBD.

Table 1 Selected bon lengths (Å) and angles (°) for cations **1**, **3**, and **5**

	1	**3**	**5**
Bond lengths (Å)			
Ru1–P (21or 23)	2.300(2)	2.3031(13)	2.3098(9)
Ru1–N7	2.090(7)	2.080(4)	2.098(3)
Ru1–N18	2.101(6)	2.095(4)	2.089(3)
Ru1–Cp (centroid)	1.842(4)	1.829(2)	1.826(2)
Angles (°)			
N18–Ru1–N7	76.5(3)	76.04(16)	78.06(10)
N18–Ru1–P (21or 23)	89.49(17)	88.39(11)	88.50(7)
N7–Ru1–P (21or 23)	87.73(19)	89.17(11)	88.32(7)
Cp(centroid)–Ru1–N18	127.6 (2)	128.84(15)	128.40(9)
Cp(centroid)–Ru1–N7	133.2(3)	131.15(15)	130.73(9)
Cp(centroid)–Ru1–P (21 or 23)	124.98(15)	126.82(9)	126.95(6)

Fig. 2 ORTEP plots and labeling schemes for the cations of complexes **1** (A), **3** (B), and **5** (C).

The distances between the ruthenium centers and the centroids of the cyclopentadienyl rings range from 1.826(2) to 1.842(4) Å, consistent with values reported for similar compounds in the literature.[35,37] A similar trend is observed for the Ru–P bond lengths, which fall within the range of 2.300(2)–2.3098(9) Å. Notably, for the compounds containing bipyridyl ligands (**1**, **3**), the Ru–N bond distances remain largely unaffected by the nature of the substituents on the bipyridyl ring. However, in compound **5**, which features a phenanthroline ligand, a slight increase in Ru–N bond lengths is observed compared to the previous two complexes (see Table 1). All compounds exhibit weak intramolecular hydrogen bonding interactions between the nitrogen atoms of the piperazine substituent (adjacent to the phosphorus atoms) and two hydrogen atoms from the cyclopentadienyl rings.

These values range from 2.737(15) to 3.127(11) Å, and an example of this type of interaction is illustrated in Fig. S18 of the SI.

The bond angles between donor atoms around the Ru center are comparable to those reported for other cyclopentadienyl-based complexes in the literature.[36] In general, the Cp(centroid)–Ru–N angles are larger than the Cp(centroid)–Ru–P angles, likely due to the steric constraints imposed by the substituents on the phosphine ligand. For all complexes, the N–Ru–N angles reflect the geometric constraints inherent to the bipyridyl and phenanthroline ligands.

The packing structures of the compounds are shown in Fig. S19–S21 of the SI. Interestingly, the unit cells of all the described compounds exhibit a centre of inversion, which plays a significant role in determining the molecular packing. In compound **1**, the packing along the *a*-axis reveals molecular chains in which all the molecules adopt the same orientation along the chain. However, alternating orientation is observed between adjacent chains (Fig. S19 of the SI). This intra-chain arrangement appears to be influenced by intermolecular hydrogen bonding, both between neighbouring molecules and between molecules and PF_6^- anions, which, along with solvent molecules, are located between the chains. These intermolecular interactions involve hydrogen atoms from phenyl and methylene groups of the phosphane substituents forming hydrogen bonds with oxygen atoms from the NO_2 group of neighbouring molecules (H22D–O40 Å = 2.555(11) Å; H46–O40 Å = 2.613(12) Å). Additional hydrogen bonds are observed between PF_6^- counterions and hydrogens from the phenyl and bipyridyl rings of two adjacent molecules of two different chains (H50–F3S = 2.546(12) Å; H16A–F4S = 2.558(12) Å) (Fig. S19B of the SI). A similar intra-chain arrangement is observed in the packing of compound **3** along the *a*-axis (Fig. S20 of the SI), consistent with the presence of analogous intermolecular interactions in both complexes, as seen in compound **1**. The molecular packing of **5** along the *a*-, *b*-, and *c*-axes is shown in Fig. S21 of the SI.

Stability of the complexes

Studies in organic and aqueous relevant media with the new 'RuCp' complexes bearing bipyridine-based ligands were performed before *in vitro* evaluation to assess their stability in solution. The stability of all NDB-labelled 'RuCp' complexes was examined *via* both NMR and UV-Vis spectroscopy. A series of ^1H and $^{31}P\{^1H\}$ NMR spectra were recorded in DMSO-d_6 solution throughout 24 h. No variation of the chemical shift values of the characteristic peaks of complexes **1–5** was noticed, meaning that these complexes are highly stable in DMSO-d_6 (Fig. S22 of the SI). This was further confirmed by UV-Vis spectroscopy (under shaded conditions), which remained unchanged over 24 hours (data not shown).

The stability of the cationic complexes was also evaluated in aqueous cell culture medium DMEM without phenol red. Complexes **1–5** were first solubilized in DMSO and then diluted to 5% DMSO with DMEM. Changes in shape or intensity are negligible over 24 h (absorbance variations below 10%, Fig. S23 of the SI). Overall, this set of compounds is robust regarding ligand exchange, maintaining the original structure over time, which is a highly desirable feature in this context.

Anticancer activity of the compounds on cancer and non-cancerous cell lines

To assess the anticancer activity of the new Ru(II) compounds, their cytotoxicity was evaluated in three cancer cell lines of different histological origins, selected for being among the most commonly used models in the screening of new candidates: 4T1 (murine epithelial breast cancer), CT26 (murine colon carcinoma), and U2OS (human osteosarcoma) – as well as in one normal cell line, 3T3 (murine embryonic fibroblasts).[38]

Cells were incubated with complexes **1–5**, Ph_2P-CH_2-pip-NBD and cisplatin (CDDP), and cell viability was assessed after a 48 h period, and their cytotoxicity (IC_{50} values) was determined using the Alamar blue assay. The cytotoxicity analysis revealed distinct variations in the toxicity of the tested compounds across the different cell lines. Complex **1** exhibited the highest cytotoxic effects in all cell lines tested, with low IC_{50} values, particularly in 4T1 (7.42 ± 0.63 µM) and U2OS (3.73 ± 0.28 µM). Complexes **2** and **5** also demonstrated significant toxicity, particularly in U2OS (IC_{50} = 4.57 ± 0.46 and IC_{50} = 6.94 ± 1.70 µM, respectively). 3T3 fibroblast also demonstrated moderate sensitivity to these compounds, with IC_{50} values for complexes **1** and **3** (IC_{50} = 7.58 ± 0.16 µM and IC_{50} = 13.00 ± 0.67 µM, respectively) comparable to those observed in cancer cells, thus suggesting potential off-target effects. On the other hand, **2** and **4** did not display significant toxicity, with IC_{50} values exceeding 100 µM in all tested cell lines (Table 2 and Fig. S24–S27 of the SI). This indicates that the incorporation of hydroxyl or biotin substituents on the bipyridine ligand has a detrimental impact on cytotoxic activity within this compound family. A similar trend has been previously reported for related systems.[35,37]

The most unexpected observation was the response of CT26 cells to the organometallic complexes, as they exhibited markedly higher resistance, with IC_{50} values exceeding 100 µM for all tested compounds, except for complex **1**, which showed a comparatively high IC_{50} of 23.21 ± 0.17 µM relative to its

Table 2 IC$_{50}$ values (µM) of complexes **1–5**, Ph$_2$P-CH$_2$-pip-NBD, and cisplatin (CDDP) measured after 48 h incubation with increasing concentrations (0–100 µM) of each compound in murine epithelial breast cancer (4T1), murine colon carcinoma (CT26), human osteosarcoma (U2OS), and murine embryonic fibroblasts (3T3) cell lines, using the Alamar blue assay. Data are means $\pm$ standard error of the mean (SEM) (n = 3)

	4T1	CT26	U2OS	3T3
1	7.42 ± 0.63	23.21 ± 0.17	3.73 ± 0.28	7.58 ± 0.16
2	>100	>100	>100	>100
3	11.14 ± 2.08	>100	4.57 ± 0.46	13.00 ± 0.67
4	>100	>100	>100	>100
5	12.14 ± 1.23	>100	6.94 ± 1.70	19.59 ± 3.73
Ph$_2$P-CH$_2$-pip-NBD	43.06 ± 3.7	15.61 ± 0.56	48.83 ± 3.29	14.49 ± 0.79
CDDP	8.68 ± 0.90	15.46 ± 4.96	16.86 ± 5.07	9.94 ± 0.38

effects on other cancer cell lines. These observations may be explained by the high mutational load of CT26 cells.[38] Overall, **1**, **3**, and **5** demonstrated significantly higher cytotoxicity than the Ph$_2$P-CH$_2$-pip-NBD fluorescent ligand (except for CT26 cells), highlighting these candidates as the most promising compounds. Additionally, these compounds showed similar cytotoxicity to cisplatin (with the exception of CT26 cells), being particularly more cytotoxic in the human osteosarcoma U2OS cell line.

Cellular uptake studies

Next, we investigated the cellular internalization of the compounds to determine whether their cytotoxicity was linked to differences in their ability to be internalized by target cells. Cell uptake was measured by flow cytometry, taking advantage of the compounds' intrinsic fluorescence. Since all complexes share similar absorption and emission spectra, with maximum absorption at λ_{max} ~490 nm and peak emission at λ_{em} ~550 nm in DMSO (Fig. S17 of the SI), as well as comparable fluorescence quantum yields (Table S1 of the SI), we were able to directly compare cell uptake of the complexes by measuring their fluorescence associated with the cells. However, it is important to note that, while all organometallic complexes exhibit very low fluorescence quantum yields, the precursor Ph$_2$P-CH$_2$-pip-NBD shows the highest Φ_F. This suggests that the presence of the 'RuCp' scaffold reduced the overall fluorescence signal.

Cells were incubated with complexes **1–5** at concentrations of 6.25 µM and 12.5 µM for 25 h and, after a washing step, immediately analyzed by flow cytometry (Fig. 3A and B). The gating and fluorescence histograms obtaining by flow cytometry are shown in Fig. S28–S35 of the SI. Complexes **1**, **3**, and **5** exhibited the highest cell uptake across all cell lines, whereas complexes **2** and **4** demonstrated the lowest levels of internalization. This trend in cell uptake correlates well with the compounds' cytotoxicity. Notably, U2OS, the most sensitive cell line to complexes **1**, **3**, and **5** (cell uptake could not be recorded for complexes **1** and **3** at 12.5 µM due to high toxicity), showed the highest internalization of these complexes. However, it should be noted that the correlation between cell uptake and cytotoxicity was not observed in CT26 cells. In these cells, cell uptake was similar to that in other cell lines, but no significant toxicity (except for complex **1**) was detected. Overall, a strong

correlation between cell uptake and cytotoxicity was observed in 4T1, U2OS, and 3T3 cells, but not in CT26 cells, suggesting that these cells may possess more robust defense mechanisms against cell death mediated by the complexes. To confirm that all complexes were internalized rather than merely associated with the cell membrane, fluorescent microscopy was used to image cells incubated with the compounds for 6 h. The acquired images reveal that the compounds localize within the cells, accumulating in cytoplasmic dots and with some dispersed signal throughout the cytoplasm (Fig. 3C).

Given the observed intracellular accumulation of the fluorescent complexes as distinct punctate dots, the most likely internalization mechanism is endocytosis – a process by which the cell membrane engulfs the compound, forming small vesicles (endosomes) that transport it into the cell. In order to confirm endocytosis as the primary internalization route, we evaluated the cellular uptake of the compounds in the presence of inhibitors of specific endocytic pathways, namely, chloroquine (a clathrin-mediated endocytosis inhibitor) and genistein (a caveolin-mediated endocytosis inhibitor). Flow cytometry and fluorescence microscopy experiments demonstrated that co-incubation of complexes **1–5** with chloroquine induced a slight, though not statistically significant, increase in the uptake of the compounds. This modest increase in intracellular accumulation may be explained by chloroquine's interference with the maturation of early endosomes into late endosomes and their subsequent fusion with lysosomes. By disrupting this trafficking pathway, chloroquine may lead to the accumulation of endosomes, thereby reducing compound degradation and contributing to increased intracellular retention (Fig. 4A and C). In contrast, genistein significantly inhibited their internalization, with a more pronounced effect observed for **1**, **3**, and Ph$_2$P-CH$_2$-pip-NBD. These results suggest that complexes **1–5** are primarily internalized via endocytosis, namely caveolin-mediated endocytosis (Fig. 4B and C).

These findings are consistent with the lack of correlation between the partition coefficients (K_P) for lipid membranes of POPC:POPS (LUVs diameter 117.5 ± 1.1 nm; zeta potential –10.3 ± 0.8 mV) and cell uptake. K_P values were determined for the Ph$_2$P-CH$_2$-pip-NBD free ligand (K_P = 3.47 × 10^2, log K_P = 2.54 ± 0.23), complex **1** (K_P = 5.80 × 10^2, log K_P = 2.76 ± 0.26), one of the compounds with higher uptake and cytotoxicity, and complex **2** (K_P = 2.64 × 10^3, log K_P = 3.42 ± 0.41), which
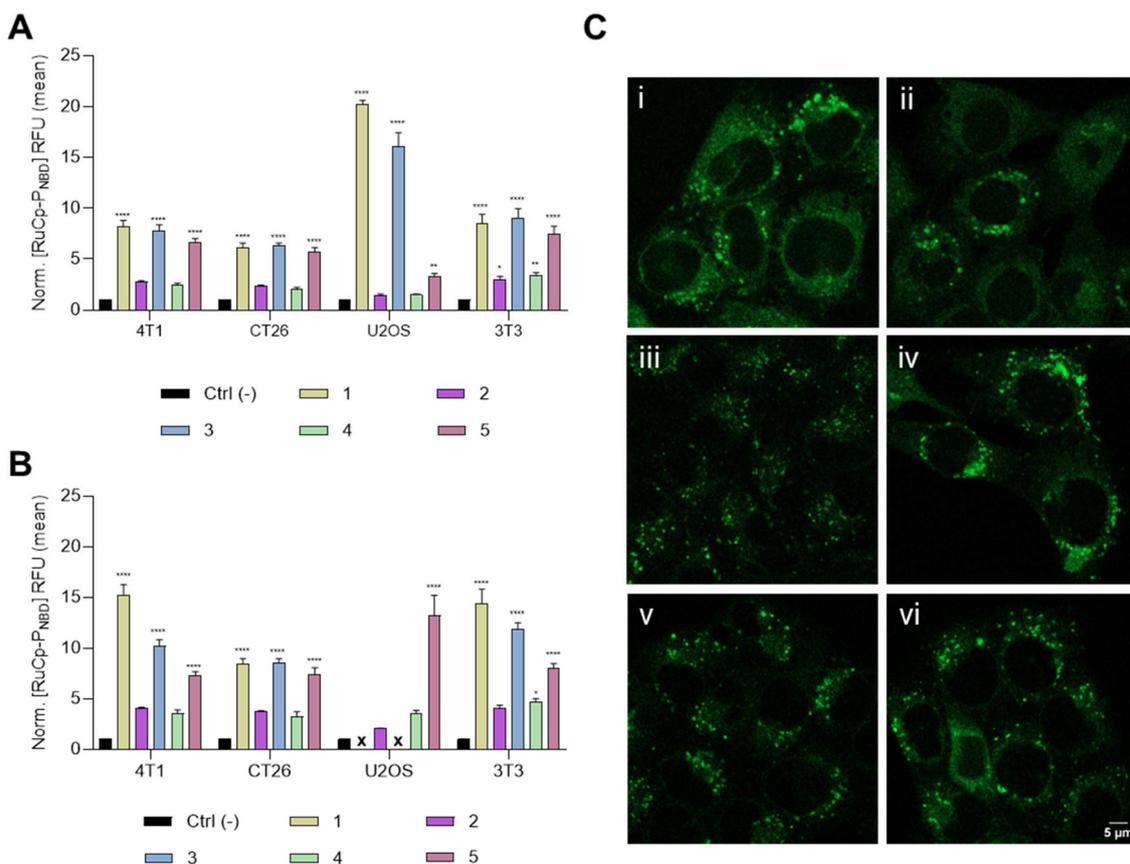
Fig. 3 Intracellular accumulation of complexes **1–5**. Cell uptake of complexes **1–5** at (A) 6.25 μM or (B) 12.5 μM through the detection of their fluorescence in 4T1, CT26, U2OS and 3T3 cells after an incubation of 25 hours. Bars indicate the mean ± standard error of the mean (SEM) of three independent experiments. In B, data for complexes **1** and **3** in U2OS cells are not shown, as all cells died after 25 hours of treatment. (C) Representative images of 4T1 cells taken 6 h after incubation with (i) Ph_2P-CH_2-pip-NBD, (ii) **1**, (iii) **2**, (iv) **3**, (v) **4**, and (vi) **5**. *$p < 0.05$, **$p < 0.01$, ****$p < 0.0001$ *vs.* ctrl (−).

exhibited one of the lowest uptake and cytotoxicity levels. The Ph_2P-CH_2-pip-NBD and complex **1** showed lower K_P values, indicating a weaker affinity for lipid membranes, while complex **2** had the highest K_P, indicating greater membrane affinity (Fig. S36 of the SI). However, these values did not correlate with the observed cellular internalization trends, as complex **1** was more efficiently internalized than complex **2** (Fig. 3). This discrepancy can be explained by the fact that K_P is expected to correlate with internalization *via* passive diffusion (which involves direct passage through the phospholipid bilayer), but not *via* endocytosis (which involves vesicular uptake). In fact, the results observed indicate an inverse correlation between the compound toxicity and its membrane affinity. The higher K_P observed for complex **2** in comparison with complex **1** is also unexpected given that the only structural difference is the presence of two CH_2OH groups in complex **2** instead of two CH_3 groups in complex **1**. It was also observed that while the fluorescence quantum yield in DMSO is only slightly higher for complex **1** (Table S1), the fluorescence increase observed upon association with the lipid membranes is 5-fold higher for this complex. This suggests

that complex **2** interacts mostly with the polar lipid headgroups and thus, its higher value of K_P is not expected to lead to a higher passive permeability.[39–41] Those results further reinforce that cell uptake of these complexes occurs mostly by endocytosis.

Intracellular localization studies

Having confirmed that the primary mechanism of cellular internalization of the new complexes is caveolin-mediated endocytosis, and considering their punctate intracellular distribution, their lysosomal tropism was further validated by confocal microscopy using Lysotracker Red as a lysosomal marker. As expected, strong colocalization between the complexes and Lysotracker Red was observed, with compounds **1** and **3** also being detected in the cytoplasm (Fig. 5).

Although the fluorescence quantum yields of the complexes were very low in DMSO (0.001 to 0.0027, Table S1 of the SI), relatively strong intracellular fluorescence was observed in our experiments using flow cytometry and fluorescence microscopy (Fig. 3–5). This was particularly evident when the compounds were localized in endosomes and/or lysosomes, which are
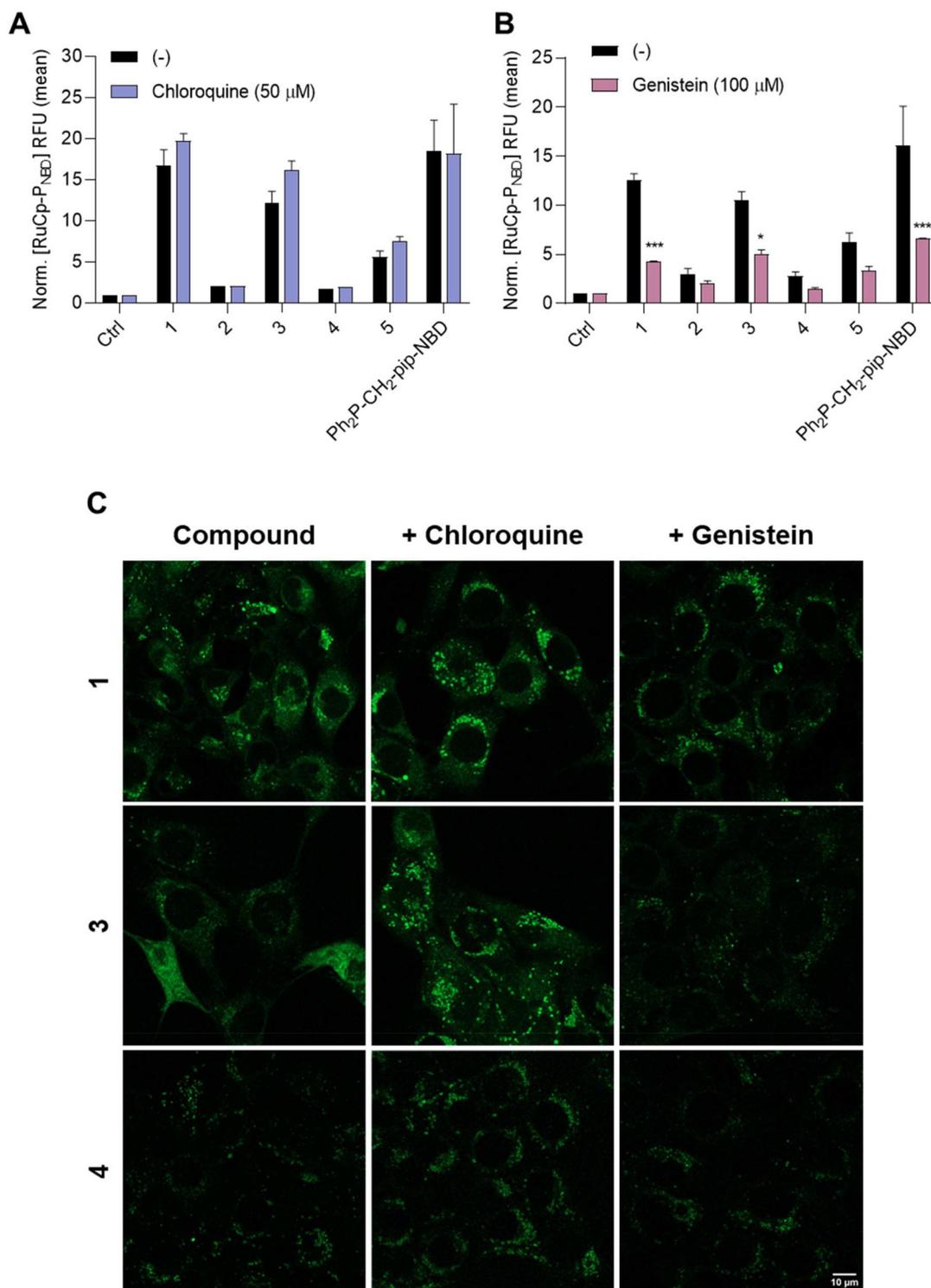
Fig. 4 Fluorescent Ru(II)–cyclopentadienyl complexes are internalized by caveolin-mediated endocytosis. Cell uptake of fluorescent compounds by 4T1 cells in the presence of (A) chloroquine (50 μM); [**1–5** and Ph$_2$P-CH$_2$-pip-NBD = 12.5 μM] or (B) genistein (100 μM); [**1–5** and Ph$_2$P-CH$_2$-pip-NBD = 9 μM], assessed by flow cytometry after 6–7 h of incubation. Bars represent the mean ± standard error of the mean (SEM) of two (or three) independent experiments. (C) Representative images of 4T1 cells taken 6 h after incubation with **1**, **3**, and **4** in presence of chloroquine (50 μM) or genistein (100 μM). *$p < 0.05$, ***$p < 0.001$ *vs.* ctrl.
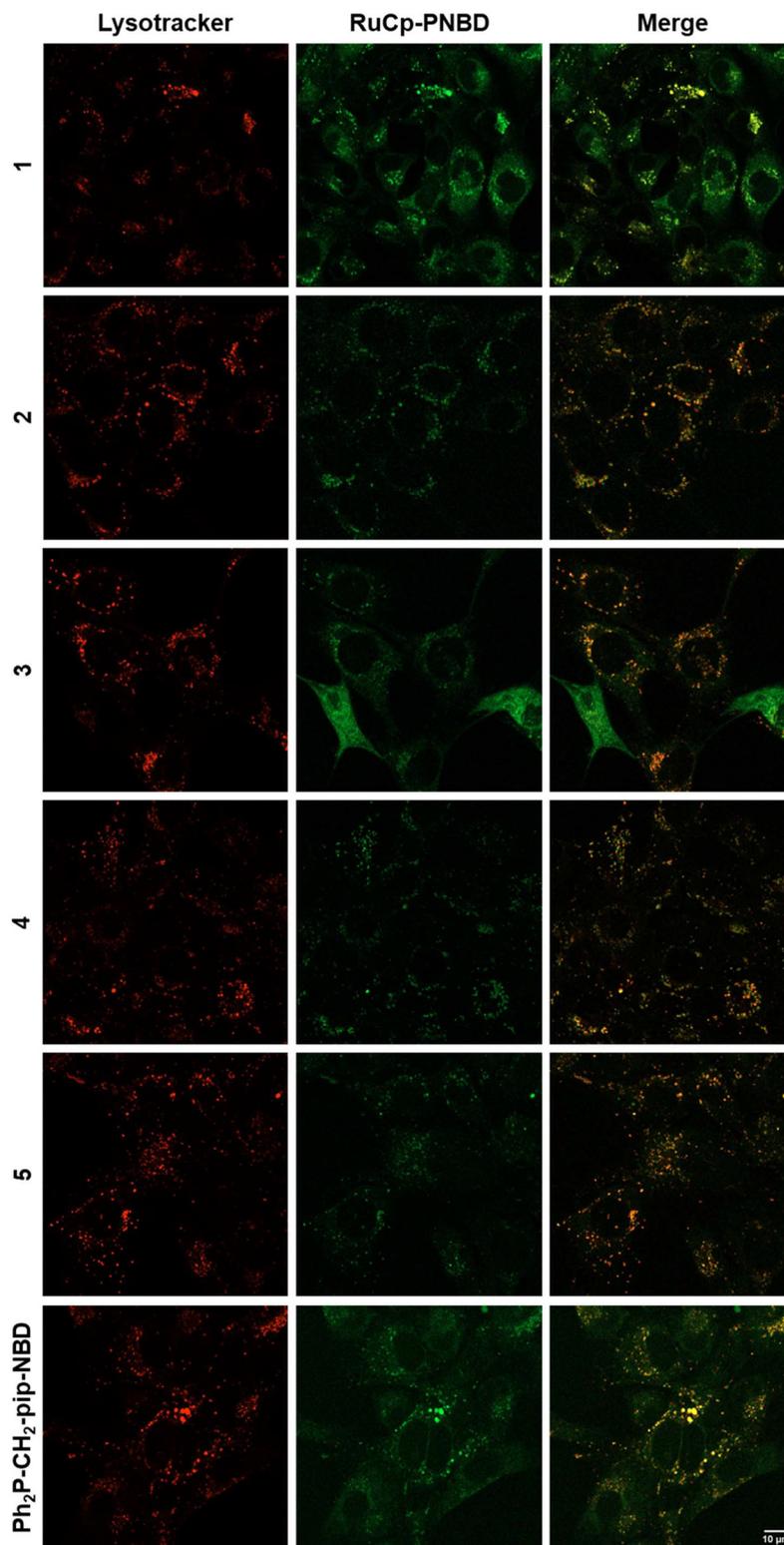
Fig. 5 Ru(II)–cyclopentadienyl complexes (in green) mainly accumulate in lysosomes (in red). Representative images of 4T1 cells taken 6 h after incubation with complexes **1–5** and Ph$_2$P-CH$_2$-pip-NBD.

acidic compartments. These findings suggest that, like the free Ph$_2$P-CH$_2$-pip-NBD ligand, complexes **1–5** may exhibit enhanced fluorescence at acidic pH.[24] Indeed, a kinetic study

conducted at different pH values (2, 6, and 7.4) revealed a significant increase in the fluorescence of **1** and **2** at pH 2, but not at pH 6 or 7.4. The fluorescence of Ph$_2$P-CH$_2$-pip-NBD was

much higher at pH 2, even at small times after incubation at this pH, with a more moderate and slower increase at pH 6 (Fig. S37 of the SI). A very strong fluorescence increase was observed for complex **1** when at pH 2, occurring over 7 hours and stabilizing at the fluorescence intensity observed for Ph_2P-CH_2-pip-NBD, while no variation was observed at pH 6 or 7.4. A similar behavior was observed for complex **2**, although with slower kinetics. The enhanced fluorescence at acidic pH may be due to the protonation of the amino groups in the complexes. Additionally, one cannot neglect the possibility of Ph_2P-CH_2-pip-NBD release from the ruthenium complex within the lysosomes, leading to increased fluorescence, as the quantum yield of Ph_2P-CH_2-pip-NBD is 5 to 10 times higher than that of the Ru complexes.

ROS detection and morphological indicators of apoptosis

To gain further insight into the mechanism of action of the most cytotoxic compounds, the overall level of oxidative stress was indirectly assessed using the CellROX™ Deep Red reagent, which becomes fluorescent upon oxidation. A significant increase in oxidative stress was observed in cells treated with compounds **1**, **3** and **5** (Fig. S38 of the SI), suggesting that these compounds may promote the production of reactive oxygen species (ROS), as reported for several families of ruthenium complexes.[42–44] This enhanced oxidative stress is expected to contribute to cell death, whose mechanism was further investigated in 4T1 cells by microscopy. Hallmarks of apoptosis, including cell shrinkage, formation of apoptotic bodies, and chromatin condensation and fragmentation, were evident after 6 h of incubation and became more pronounced after 24 and 48 h, particularly for compounds **1** and **3**, indicating that apoptosis is the main mechanism of cell death induced by this class of compounds (Fig. S39 of the SI).

Conclusions

In this study, we successfully synthesized and characterized a new family of luminescent ruthenium(ɪɪ)–cyclopentadienyl complexes incorporating an NBD-functionalized phosphane ligand. The introduction of the Ph_2P-CH_2-pip-NBD unit conferred intrinsic fluorescence as desired and enabled subcellular tracking without compromising the structural integrity or cytotoxic properties of the organometallic scaffold. Detailed spectroscopic and crystallographic analyses confirmed the expected coordination geometry, while stability assays demonstrated the robustness of the complexes under mimetic physiological conditions. Biological evaluation revealed that complexes **1**, **3**, and **5** possess significant anticancer activity, particularly against the U2OS cell line, with cytotoxicity profiles that correlate with their cellular uptake. Mechanistic insights indicated that internalization proceeds primarily *via* caveolin-mediated endocytosis, and colocalization studies confirmed selective lysosomal accumulation. Furthermore, the pH-dependent enhancement of fluorescence suggests a lysosome-activated imaging capability, reinforcing their potential as lysosome-targeted

agents. ROS generation and apoptosis seem also to be key contributors to the cytotoxic activity of this compounds' family. Taken together, these results highlight the potential of this fluorescent 'RuCp' platform as a promising hit for the development of traceable, organelle-targeted anticancer metallodrugs.

Methods

Materials

All chemicals were purchased from commercial sources and used without further purification (unless otherwise stated). $[Ru(\eta^5-C_5H_5)(NCCH_3)_3][PF_6]$ was purchased from Sigma-Aldrich and used without further purification. Ph_2P-CH_2-pip-NBD ligands was prepared according to published methods.[24]

Instrumentation and methods (experimental section)

General procedures

All reactions and purification of compounds were performed under nitrogen atmosphere using Schlenk techniques. Dichloromethane, THF and *n*-hexane were dried using an MBRAUN solvent purification system (MB SPS-800, M Braun Inertgas-Systeme GmbH, Garching, Germany). NMR spectra were recorded on a Bruker Avance 400 spectrometer at probe temperature (298 K) using commercially available deuterated acetone and dimethylsulfoxide. Chemical shifts (δ) are reported in parts per million (ppm) referenced to tetramethylsilane (δ 0.00 ppm) using the residual proton solvent peaks as internal standards. The multiplicity of the peaks is abbreviated as follows: s (singlet), d (doublet), t (triplet), m (multiplet). Coupling constants (J) are reported in Hertz (Hz). All assignments were attributed using COSY, HMBC, and HMQC bidimensional-NMR techniques. Infrared spectra were recorded on KBr pellets using a Mattson Satellite FT-IR spectrophotometer. Only considered relevant bands were cited in the text. Electronic spectra were recorded at room temperature on a Jasco V-660 spectrometer from solutions of 10^{-4}–10^{-6} M in quartz cuvettes (1 cm optical path), under air and at room temperature. Elemental analyses were performed at *Laboratório de Análises*, at *Instituto Superior Técnico*, using a Fisons Instruments EA1 108 system. ESI-MS data acquisition, integration and handling were performed using a PC with the software package EAGER-200 (Carlo Erba Instruments).

Synthesis of the ruthenium complexes

Compounds of general formula $[Ru(\eta^5-C_5H_5)(NN)(Ph_2P-CH_2-NBD)][PF_6]$ (**1–5**) were obtained by addition of 4,4′-dimethyl-2,2′-bipyridine (for **1**; 32 mg, 0.17 mmol), 4,4′-bis(hydroxymethyl)-2,2′-bipyridine (for **2**; 37 mg, 0.17 mmol), 4,4′-dimethoxy-2,2′-bipyridine (for **3**; 37 mg, 0.17 mmol), 2,2′-bipy-4,4′-dibiotin ester (for **4**; 116 mg, 0.17 mmol) or 1,10-phenanthroline (for **5**; 31 mg, 0.17 mmol) to a stirred solution of the cationic complex $[Ru(\eta^5-C_5H_5)(NCCH_3)_3][PF_6]$ (75 mg,

0.17 mmol) in dichloromethane (10 mL) cooled with ice/water bath (0 °C). Afterwards, Ph$_2$P-CH$_2$-pip-NBD (78–80 mg, 0.17–0.18 mmol) was added, and the solution was warmed up to room temperature slowly and stirred for 4 h while protected from light exposure. Compounds **3** and **5** separate from the mixture as orange solids as the reaction goes on. After evaporation of the solvent, the dark-reddish residue was recrystallized from slow diffusion of *n*-hexane into dichloromethane (for **1** and **3**) or THF (for **2**) solutions of from diffusion of diethyl ether into acetonitrile solution (for **5**), affording dark red or orange crystalline solids.

Optimized synthesis of complex 4

[Ru(η^5-C$_5$H$_5$)(4,4′-CH$_2$OH-2,2′-bipy)(Ph$_2$P-CH$_2$-pip-NBD)][PF$_6$] (**2**; 80 mg, 0.08 mmol) was combined with 5-[(3a*S*,4*S*,6a*R*)-2-oxohexahydro-1*H*-thieno[3,4-*d*]imidazol-4-yl]pentanoic acid (Biotin; 50 mg, 0.2 mmol), 4-dimethylaminopyridine (DMAP; 6 mg; 0.05 mmol) and EDC·Cl (39 mg, 0.2 mmol) in a Schlenk and dimethylformamide (DMF; 5 mL) was added. The orange mixture was stirred for 14 h at room temperature. On the next day, the solvent was removed under vacuum and the residue obtained washed with water (10 mL × 3) and diethyl ether (10 mL × 3), to yield an orangish red solid.

[Ru(η^5-C$_5$H$_5$)(phen)(Ph$_2$P-CH$_2$-pip-NBD)][PF$_6$] (1). Single crystals were obtained from slow evaporation of an acetone solution.

Yield: 93%. ^{1}HNMR [(CD$_3$)$_2$CO, Me$_4$Si] δ (ppm): 9.22 (d, 2H, $^3J_{HH}$ = 6, H6^{bipy}), 8.43 (d, 1H, $^3J_{HH}$ = 9, H5$^{'PPh2-CH2-pip-NBD}$), 7.90 (s, 2H, H3^{bipy}), 7.37 (m, 2H, $^3J_{HH}$ = 7, H$_{para}$$^{PPh2-CH2-pip-NBD}$), 7.21 (m, 6H, H$_{meta}$$^{PPh2-CH2-pip-NBD}$ + H5^{bipy}), 7.09 (t, 4H, $^3J_{HH}$ = 8, H$_{ortho}$$^{PPh2-CH2-pip-NBD}$), 6.57 (d, 1H, $^3J_{HH}$ = 9, H6$^{'PPh2-CH2-pip-NBD}$), 5.11 (s, 5H, C$_5$H$_5$), 4.00 (m, 4H, H3$^{PPh2-CH2-pip-NBD}$ + H5$^{PPh2-CH2-pip-NBD}$), 3.79 (s, 2H, PPh$_2$-CH$_2$-pip-NBD), 2.62 (t, 4H, $^3J_{HH}$ = 5, H2$^{PPh2-CH2-pip-NBD}$ + H6$^{PPh2-CH2-pip-NBD}$), 2.45 (s, 6H, CH$_3$^{bipy}). APT-^{13}C{^{1}H} NMR [(CD$_3$)$_2$CO] δ (ppm): 156.3 (C6^{bipy}), 156.0 (C2^{bipy}), 149.0, (C4^{bipy}), 146.1 (C1$^{'Ph2P-CH2-pip-NBD}$), 146.0 + 145.8 (C2$^{'Ph2P-CH2-pip-NBD}$ + C3$^{'Ph2P-CH2-pip-NBD}$), 136.3 (C5$^{'Ph2P-CH2-pip-NBD}$), 133.5 (d, $^2J_{CP}$ = 11, CH$_{ortho}$$^{Ph2P-CH2-pip-NBD}$), 131.8 (d, $^1J_{CP}$ = 38, C$_{ipso}$$^{Ph2P-CH2-pip-NBD}$), 130.6 (d, $^4J_{CP}$ = 2, CH$_{para}$$^{Ph2P-CH2-pip-NBD}$), 129.1 (d, $^3J_{CP}$ = 10, CH$_{meta}$$^{Ph2P-CH2-pip-NBD}$), 127.1 (C5^{bipy}), 124.7 (C3^{bipy}), 104.2 (C6$^{'Ph2P-CH2-pip-NBD}$), 77.6 (d, $^2J_{CP}$ = 2, C$_5$H$_5$), 60.9 (d, $^1J_{CP}$ = 38, C1$^{Ph2P-CH2-pip-NBD}$), 55.7 (d, $^3J_{CP}$ = 9, C2$^{Ph2P-CH2-pip-NBD}$ and C6$^{Ph2P-CH2-pip-NBD}$), 50.1 (C3$^{Ph2P-CH2-pip-NBD}$ and C5$^{Ph2P-CH2-pip-NBD}$), 20.8 (CH$_3$). ^{31}P{^{1}H} NMR [(CD$_3$)$_2$CO] δ (ppm): 45.5 (s, Ph$_2$P-CH$_2$-pip-NBD), −144.3 (sept, $^1J_{PF}$ = 708, PF$_6$). FTIR [KBr, cm^{-1}]: 3053 (νC–H aromatic rings), 2921–2852 (νC–H alkanes), 1617 and 1436 (νC=C aromatic rings), 843 and 557 (νPF$_6$ counterion). UV-Vis [NCCH$_3$, λ$_{max}$/nm (ε × 10^3/ M^{-1} cm^{-1})]: 238 (sh), 290 (4.3), 340 (2.9), 481 (5.8). Elemental analysis calc. for C$_{40}$H$_{39}$F$_6$N$_7$O$_3$P$_2$Ru (942.79): C, 50.96, H, 4.17; N, 10.40. Found: C 51.1; H, 4.2; N, 10.2. ESI-MS: [**1**-PF$_6$]$^+$ calc. for [C$_{40}$H$_{39}$N$_7$O$_3$PRu]$^+$: 797.83. Found: 797.98.

[Ru(η^5-C$_5$H$_5$)(bipy(CH$_2$OH)$_2$)(Ph$_2$P-CH$_2$-pip-NBD)][PF$_6$] (2). Yield: 81%. ^{1}H NMR [(CD$_3$)$_2$CO, Me$_4$Si] δ (ppm): 9.34 (d, 2H,

$^3J_{HH}$ = 6, H6^{bipy}), 8.43 (d, 1H, $^3J_{HH}$ = 9, H5$^{'P2P-CH2-pip-NBD}$), 7.98 (s, 2H, H3^{bipy}), 7.37 (m, 4H, $^3J_{HH}$ = 7, H$_{para}$$^{PPh2-CH2-pip-NBD}$ + H5^{bipy}), 7.21 (m, 4H, H$_{meta}$$^{PPh2-CH2-pip-NBD}$), 7.09 (t, 4H, $^3J_{HH}$ = 8, H$_{ortho}$$^{PPh2-CH2-pip-NBD}$), 6.57 (d, 1H, $^3J_{HH}$ = 9, H6$^{'P2P-CH2-pip-NBD}$), 5.15 (s, 5H, C$_5$H$_5$), 4.77 (m, 6H, CH$_2$OH^{bipy}), 4.01 (m, 4H, H3$^{Ph2P-CH2-pip-NBD}$ + H5$^{Ph2P-CH2-pip-NBD}$), 3.78 (s, 2H, Ph$_2$P-CH$_2$-pip-NBD), 2.62 (t, 4H, $^3J_{HH}$ = 5, H2$^{Ph2P-CH2-pip-NBD}$ + H6$^{Ph2P-CH2-pip-NBD}$). APT-^{13}C{^{1}H} NMR [(CD$_3$)$_2$CO] δ (ppm): 156.4 (d, $^3J_{CP}$ = 2, C6^{bipy}), 156.1 (C4^{bipy}), 153.4 (C6^{bipy}), 146.1 (C1$^{'Ph2P-CH2-pip-NBD}$), 146.0 + 145.8 (C2$^{'Ph2P-CH2-pip-NBD}$ + C3$^{'Ph2P-CH2-pip-NBD}$), 136.3 (C5$^{'Ph2P-CH2-pip-NBD}$), 133.4 (d, $^2J_{CP}$ = 11, CH$_{ortho}$$^{Ph2P-CH2-pip-NBD}$), 131.6 (d, $^1J_{CP}$ = 38, C$_{ipso}$$^{Ph2P-CH2-pip-NBD}$), 130.7 (d, $^4J_{CP}$ = 2, CH$_{para}$$^{Ph2P-CH2-pip-NBD}$), 129.1 (d, $^3J_{CP}$ = 10, CH$_{meta}$$^{Ph2P-CH2-pip-NBD}$), 123.5 (C5^{bipy}), 120.9 (C3^{bipy}), 104.2 (C6$^{'Ph2P-CH2-pip-NBD}$), 77.7 (d, $^2J_{CP}$ = 2, C$_5$H$_5$), 62.5 (CH2^{bipy}), 59.8 (d, $^1J_{CP}$ = 38, C1$^{Ph2P-CH2-pip-NBD}$), 55.7 (d, $^3J_{CP}$ = 9, C2$^{Ph2P-CH2-pip-NBD}$ and C6$^{Ph2P-CH2-pip-NBD}$), 50.1 (C3$^{Ph2P-CH2-pip-NBD}$ and C5$^{Ph2P-CH2-pip-NBD}$). ^{31}P{^{1}H} NMR [(CD$_3$)$_2$CO] δ (ppm): 45.5 ppm (s, PPh$_2$-CH$_2$-pip-NBD), −144.3 (sept, $^1J_{PF}$ = 708, PF$_6$). FTIR [KBr, cm^{-1}]: 3444 (νO–H), 3078–3058 (νC–H aromatic rings), 2925–2854 (νC–H alkanes), 1612 and 1436 (νC=C aromatic rings), 1332 (νN–O), 1132 (νC–O), 847 and 558 (νPF$_6$ counterion). UV-Vis [NCCH$_3$, λ$_{max}$/nm (ε × 10^3/M^{-1} cm^{-1})]: 238 (sh), 290 (4.1), 339 (2.6), 480 (5.1). Elemental analysis calc. for C$_{40}$H$_{39}$F$_6$N$_7$O$_5$P$_2$Ru (974.79): C, 49.29, H, 4.03; N, 10.06. Found: C, 49.5; H, 4.2; N, 10.0. ESI-MS: [**2**-PF$_6$]$^+$ calc. for [C$_{40}$H$_{39}$N$_7$O$_5$PRu]$^+$: 829.83. Found: 829.98.

[Ru(η^5-C$_5$H$_5$)(MeO$_2$bipy)(Ph$_2$P-CH$_2$-pip-NBD)][PF$_6$] (3). Single crystals were obtained from slow diffusion of *n*-hexane into dichloromethane solution. Yield: 90%.

^{1}H NMR [(CD$_3$)$_2$CO, Me$_4$Si] δ (ppm): 9.13 (d, 2H, $^3J_{HH}$ = 6, H6^{bipy}), 8.43 (d, 1H, $^3J_{HH}$ = 9, H5$^{'Ph2P-CH2-pip-NBD}$), 7.62 (s, 2H, H3^{bipy}), 7.39 (m, 2H, $^3J_{HH}$ = 7, H$_{para}$$^{Ph2P-CH2-pip-NBD}$), 7.23(m,4H, H$_{meta}$$^{Ph2P-CH2-pip-NBD}$), 7.13 (t, 4H, $^3J_{HH}$ = 8, H$_{ortho}$$^{Ph2P-CH2-pip-NBD}$), 7.00 (dd, 2H, H5^{bipy}), 6.57 (d, 1H, $^3J_{HH}$ = 9, H6$^{Ph2P-CH2-pip-NBD}$), 5.05 (s, 5H, C$_5$H$_5$), 4.01 (m, 4H, H3$^{Ph2P-CH2-pip-NBD}$ + H5$^{Ph2P-CH2-pip-NBD}$), 3.97 (s, 6H, OCH$_3$^{bipy}), 3.78 (s, 2H, Ph$_2$P-CH$_2$-pip-NBD), 2.62 (t, 4H, $^3J_{HH}$ = 5, H2$^{Ph2P-CH2-pip-NBD}$ + H6$^{Ph2P-CH2-pip-NBD}$).

APT-^{13}C{^{1}H} NMR [(CD$_3$)$_2$CO] δ (ppm): 166.2 (C2^{bipy}), 156.8 (C4^{bipy}), 156.7 (d, $^3J_{CP}$ = 2, C6^{bipy}), 145.3 (C1$^{'Ph2P-CH2-pip-NBD}$), 145.1 + 145.0 (C2$^{'Ph2P-CH2-pip-NBD}$ + C3$^{'Ph2P-CH2-pip-NBD}$), 135.4 (C5$^{'Ph2P-CH2-pip-NBD}$), 132.7 (d, $^2J_{CP}$ = 11, CH$_{ortho}$$^{Ph2P-CH2-pip-NBD}$), 131.4 (d, $^1J_{CP}$ = 38, C$_{ipso}$$^{Ph2P-CH2-pip-NBD}$), 129.7 (d, $^4J_{CP}$ = 2, CH$_{para}$$^{Ph2P-CH2-pip-NBD}$), 128.3 (d, $^3J_{CP}$ = 10, CH$_{meta}$$^{Ph2P-CH2-pip-NBD}$), 112.5 (C5^{bipy}), 109.2 (C3^{bipy}), 103.3 (C6$^{'Ph2P-CH2-pip-NBD}$), 76.0 (d, $^2J_{CP}$ = 2, C$_5$H$_5$), 60.9 (d, $^1J_{CP}$ = 38, C1$^{Ph2P-CH2-pip-NBD}$), 59.0 (d, $^1J_{CP}$ = 38, C1$^{Ph2P-CH2-pip-NBD}$), 56.0 (OCH$_3$), 54.9 (d, $^3J_{CP}$ = 9, C2$^{Ph2P-CH2-pip-NBD}$ and C6$^{Ph2P-CH2-pip-NBD}$), 49.2 (C3$^{Ph2P-CH2-pip-NBD}$ and C5$^{Ph2P-CH2-pip-NBD}$). ^{31}P{^{1}H} NMR [(CD$_3$)$_2$CO] δ (ppm): 46.2 ppm (s, Ph$_2$P-CH$_2$-pip-NBD), −144.3 (sept, $^1J_{PF}$ = 708, PF$_6$). FTIR [KBr, cm^{-1}]: 3086–3052 (νC–H aromatic rings), 2939–2805 (νC–H alkanes), 1614 and 1436 (νC=C aromatic rings), 1129 (νC–

O), 842 and 557 (νPF_6 counterion). UV-Vis [NCCH$_3$, λ_{max}/nm ($\varepsilon \times 10^3$/M^{-1} cm^{-1})]: 236 (sh), 291 (4.7), 340 (2.7), 480 (5.6). Elemental analysis calc. for C$_{40}$H$_{39}$F$_6$N$_7$O$_5$P$_2$Ru (974.79): C, 49.29, H, 4.03; N, 10.06. Found: C, 49.4; H, 4.1; N, 10.1. ESI-MS: [3-PF$_6$]$^+$ calc. for [C$_{40}$H$_{39}$N$_7$O$_5$PRu]$^+$: 829.83. Found: 829.96.

[Ru(η^5-C$_5$H$_5$)(bipy(CH$_2$Biotin)$_2$)(Ph$_2$P-CH$_2$-pip-NBD)][PF$_6$] (4). Yield: 77%. ^{1}H NMR [(CD$_3$)$_2$CO, Me$_4$Si] δ (ppm): 9.42 (m, 2H, H6^{bipy}), 8.43 (d, 1H, $^3J_{HH}$ = 9, H5$'^{Ph2P-CH2-pip-NBD}$), 8.02 (s, 2H, H3^{bipy}), 7.40 (m, 4H, H$_{para}$$^{Ph2P-CH2-pip-NBD}$ + H5^{bipy}), 7.22 (t, 4H, $^3J_{HH}$ = 7, H$_{meta}$$^{Ph2P-CH2-pip-NBD}$), 7.08 (t, 4H, $^3J_{HH}$ = 8, H$_{ortho}$$^{Ph2P-CH2-pip-NBD}$), 6.58 (d, 1H, $^3J_{HH}$ = 9, H6$'^{Ph2P-CH2-pip-NBD}$), 6.06 (d, 2H, NH^{Biotin}), 5.87 (br d, 2H, NH^{Biotin}), 5.26 (m, 4H, CH$_2$^{Biotin}), 5.19 (s, 5H, C$_5$H$_5$), 4.49 (m, 2H, SCH$_2$CH^{Biotin}), 4.32 (m, 2H, CH^{Biotin}), 4.01 (m, 4H, H3$^{Ph2P-CH2-pip-NBD}$ + H5$^{Ph2P-CH2-pip-NBD}$), 3.82 (s, 2H, Ph$_2$P-CH$_2$-pip-NBD), 3.22 (2H, S-CH^{Biotin}), 2.63 (t, 4H, $^3J_{HH}$ = 5, H2$^{Ph2P-CH2-pip-NBD}$ + H6$^{Ph2P-CH2-pip-NBD}$), 2.50 (m, 4H, SCH$_2$Biotin), 1.78–1.49 (m, 12H, CH$_2$CH$_2$CH$_2$CH$_2$Biotin). APT-^{13}C{^{1}H} NMR [(CD$_3$)$_2$CO] δ (ppm): 173.6 (CO, bipy(CH$_2$Biotin)$_2$ ester), 164.2 (CO, bipy(CH$_2$Biotin)$_2$ urea), 156.9 (br, C6^{bipy}), 156.0 (C2^{bipy}), 147.1 (C4^{bipy}), 146.1 (C1$'^{Ph2P-CH2-pip-NBD}$), 145.9 + 145.8 (C2$'^{Ph2P-CH2-pip-NBD}$ + C3$'^{Ph2P-CH2-pip-NBD}$), 136.5 (C5$'^{Ph2P-CH2-pip-NBD}$), 133.3 (d, $^2J_{CP}$ = 11, CH$_{ortho}$$^{Ph2P-CH2-pip-NBD}$), 131.2 (d, $^1J_{CP}$ = 38, C$_{ipso}$$^{Ph2P-CH2-pip-NBD}$), 130.7 (d, $^4J_{CP}$ = 2, CH$_{para}$$^{Ph2P-CH2-pip-NBD}$), 129.2 (d, $^3J_{CP}$ = 10, CH$_{meta}$$^{Ph2P-CH2-pip-NBD}$), 124.5 (C5^{bipy}), 122.3 (C3^{bipy}), 104.2 (C6$'^{Ph2P-CH2-pip-NBD}$), 77.9 (d, $^2J_{CP}$ = 2, C$_5$H$_5$), 64.1 (CH$_2$^{bipy}), 62.4 (CH^{Biotin}), 60.7 (SCH$_2$-CHBiotin), 59.7 (d, $^1J_{CP}$ = 38, C1$^{Ph2P-CH2-pip-NBD}$), 56.5 (SCHBiotin), 59.7 (d, $^1J_{CP}$ = 38, C1$^{Ph2P-CH2-pip-NBD}$), 55.7 (d, $^3J_{CP}$ = 9, C2$^{Ph2P-CH2-pip-NBD}$ and C6$^{Ph2P-CH2-pip-NBD}$), 50.0 (C3$^{Ph2P-CH2-pip-NBD}$ and C5$^{Ph2P-CH2-pip-NBD}$), 40.9 (SCH$_2$^{Biotin}), 34.1 + 29.2* + 25 (CH$_2$CH$_2$CH$_2$CH$_2$^{Biotin})* under the solvent peak. ^{31}P{^{1}H} NMR [(CD$_3$)$_2$CO] δ (ppm): 45.31 ppm (s, Ph$_2$P-CH$_2$-pip-NBD), −144.3 (sept, $^1J_{PF}$ = 708, PF$_6$). FTIR [KBr, cm^{-1}]: 3388–3263 (νN–H), 3077 (νC–H aromatic rings), 2928–2859 (νC–H alkanes), 1732–1698 (νC=O urea, ester), 1434 (νC=C aromatic rings), 1440 (νC=C aromatic rings), 843 and 557 (νPF_6 counterion). UV-Vis [NCCH$_3$, λ/nm ($\varepsilon \times 10^3$/M^{-1} cm^{-1})]: 240 (sh), 290 (4.2), 340 (1.9), 480 (5.1). Elemental analysis calc. for C$_{60}$H$_{67}$F$_6$N$_{11}$O$_9$P$_2$RuS$_2$ (1427.38): C, 50.49, H, 4.73; N, 10.79; S, 4.49. Found: C, 50.3; H, 4.6; N, 10.6, S, 4.1. ESI MS: [4-PF$_6$]$^+$ calc. for [C$_{60}$H$_{67}$N$_{11}$O$_9$PRuS$_2$]$^+$: 1282.42. Found: 1281.99.

[Ru(η^5-C$_5$H$_5$)(phen)(Ph$_2$P-CH$_2$-pip-NBD)][PF$_6$] (5). Single crystals were obtained from slow diffusion of diethyl ether into acetonitrile solution. Yield: 87%. ^{1}H NMR [(CD$_3$)$_2$CO, Me$_4$Si] δ (ppm): 9.75 (d, 2H, $^3J_{HH}$ = 6, H2^{phen}), 8.47 (d, 2H, $^3J_{HH}$ = 6, H4^{phen}), 8.43 (d, 1H, $^3J_{HH}$ = 9, H5$'^{Ph2P-CH2-pip-NBD}$), 7.92 (s, 2H, H6^{phen}), 7.77 (m, 2H, H3^{phen}), 7.16 (t, 2H, $^3J_{HH}$ = 7, H$_{para}$$^{PPh2-CH2-pip-NBD}$), 6.97 (t, 4H, $^3J_{HH}$ = 7, H$_{meta}$$^{PPh2-CH2-pip-NBD}$), 6.90 (t, 4H, $^3J_{HH}$ = 8, H$_{ortho}$$^{Ph2P-CH2-pip-NBD}$), 6.57 (d, 1H, $^3J_{HH}$ = 9, H6$'^{Ph2P-CH2-pip-NBD}$), 5.27 (s, 5H, C$_5$H$_5$), 3.99 (m, 4H, H3$^{Ph2P-CH2-pip-NBD}$ + H5$^{Ph2P-CH2-pip-NBD}$), 3.87 (s, 2H, PPh$_2$-CH$_2$-pip-NBD), 2.62 (t, 4H, $^3J_{HH}$ = 5, H2$^{Ph2P-CH2-pip-NBD}$ + H6$^{Ph2P-CH2-pip-NBD}$). APT-^{13}C

{^{1}H} NMR [(CD$_3$)$_2$CO] δ (ppm): 156.8 (C2^{phen}), 147.6 (C5^{phen}), 145.8 (C1$'^{Ph2P-CH2-pip-NBD}$), 145.6 + 145.5 (C2$'^{Ph2P-CH2-pip-NBD}$ + C3$'^{Ph2P-CH2-pip-NBD}$), 136.0 (C5$'^{PPh2-CH2-pip-NBD}$), 135.2 (C4^{phen}), 132.5 (d, $^2J_{CP}$ = 11, CH$_{ortho}$$^{Ph2P-CH2-pip-NBD}$), 130.8 (d, $^1J_{CP}$ = 38, C$_{ipso}$$^{Ph2P-CH2-pip-NBD}$), 130.1 (d, $^4J_{CP}$ = 2, CH$_{para}$$^{Ph2P-CH2-pip-NBD}$), 128.3 (d, $^3J_{CP}$ = 10, CH$_{meta}$$^{Ph2P-CH2-pip-NBD}$), 127.6 (C6^{phen}), 125.1 (C3^{phen}), 103.8 (C6$'^{Ph2P-CH2-pip-NBD}$), 77.2 (d, $^2J_{CP}$ = 2, C$_5$H$_5$), 59.29 (d, $^1J_{CP}$ = 38, C1$^{Ph2P-CH2-pip-NBD}$), 55.4 (d, $^3J_{CP}$ = 6, C2$^{Ph2P-CH2-pip-NBD}$ and C6$^{Ph2P-CH2-pip-NBD}$), 49.7 (C3$^{Ph2P-CH2-pip-NBD}$ and C5$^{Ph2P-CH2-pip-NBD}$). ^{31}P{^{1}H} NMR [(CD$_3$)$_2$CO] δ (ppm): 46.1 (s, Ph$_2$P-CH$_2$-pip-NBD), −144.2 (sept, $^1J_{PF}$ = 708, PF$_6$). FTIR [KBr, cm^{-1}]: 3077 (νC–H aromatic rings), 2928–2859 (νC–H alkanes), 1434 (νC=C aromatic rings), 840 and 558 (νPF6 counterion). UV-Vis [NCCH$_3$, λ/nm ($\varepsilon \times 10^3$/M^{-1} cm^{-1})]: 239 (sh), 290 (4.3), 339 (2.9), 482 (5.6). Elemental analysis calc. for C$_{40}$H$_{35}$F$_6$N$_7$O$_3$P$_2$Ru (938.76): C, 51.18, H, 3.76; N, 10.44. Found: C, 51.2; H, 3.8; N, 10.7. ESI-MS: [5-PF$_6$]$^+$ calc. for [C$_{40}$H$_{35}$N$_7$O$_3$PRu]$^+$: 794.16. Found: 794.11.

Single crystal X-ray diffraction

The experimental data were measured on a Bruker D8 QUEST ECO triple-circle diffractometer system equipped with a ceramic X-ray tube (Mo Kα, λ = 0.71076 Å) and a Bruker Triumph doubly curved silicon crystal monochromator. Images were integrated using the Bruker SAINT software package (version 8.40A) with a narrow-frame algorithm. The data were corrected for absorption effects using the multi-scan method (SADABS). All structure were solved and refined using the Bruker SHELXTL Software Package (v6.14). CCDC 2476799 (for **1**), 2476798 (for **3**) and 2476797 (for **5**) contain the supplementary crystallographic data for this paper.

[Ru(η^5-C$_5$H$_5$)(Me$_2$bipy)(Ph$_2$P-CH$_2$-pip-NBD)][PF$_6$] (1). An orange, plate-like specimen of 2(C$_{40}$H$_{39}$N$_7$O$_3$PRu), 2(F$_6$P), 4.5 (C$_3$H$_6$O), approximate dimensions 0.030 mm x 0.120 mm x 0.170 mm, was used for the X-ray crystallographic analysis. A total of 1437 frames were collected. The integration of the data using a triclinic unit cell yielded a total of 184 432 reflections to a maximum θ angle of 26.57° (0.79 Å resolution), of which 18 801 were independent (average redundancy 9.810, completeness = 99.0%, R_{int} = 11.95%, R_{sig} = 6.63%) and 13 670 (72.71%) were greater than $2\sigma(F^2)$. The final cell constants of a = 11.8493(15) Å, b = 19.432(3) Å, c = 20.703(3) Å, α = 78.293(4)°, β = 77.765(5)°, γ = 84.304(5)°, volume = 4553.9(10) Å^3, are based upon the refinement of the XYZ-centroids of 9881 reflections above 20 $\sigma(I)$ with 5.350° < 2θ < 52.33°. The ratio of minimum to maximum apparent transmission was 0.950. The calculated minimum and maximum transmission coefficients (based on crystal size) are 0.9220 and 0.9860.

The structure was solved and refined using the space group $P\bar{1}$, with Z = 2 for the formula unit, C$_{93.50}$H$_{105}$F$_{12}$N$_{14}$O$_{10.50}$P$_4$Ru$_2$. The final anisotropic full-matrix least-squares refinement on F^2 with 1099 variables converged at R_1 = 10.17%, for the observed data and wR_2 = 26.16% for all data. The goodness-of-fit was 1.054. The largest peak in the final difference electron density synthesis was 2.007 e$^-$ Å^{-3} and the largest hole was −1.957 e$^-$Å^{-3} with an RMS deviation

of 0.178 e$^-$ Å^{-3}. On the basis of the final model, the calculated density was 1.566 g cm^{-3} and $F(000)$, 2208e$^-$.

The crystal lattice contained a large amount of diffuse electron density that could not be appropriately modelled. The SQUEEZE routine within PLATON was employed to resolve this problem, resulting in void electrons count per cell of 215 that was assigned to seven solvent acetone molecules. The collected data was of moderate quality, primarily due to the crystal's mosaicity. This resulted in a mixture of well-defined diffraction spots and others that were significantly broadened and poorly resolved, so the R factors are slightly higher than expected.

[Ru(η^5-C$_5$H$_5$)(MeO$_2$bipy)(Ph$_2$P-CH$_2$-pip-NBD)][PF$_6$] (3). An orange block-like specimen of C$_{42}$H$_{43}$Cl$_4$F$_6$N$_7$O$_5$P$_2$Ru, approximate dimensions 0.100 mm x 0.170 mm x 0.200 mm, was used for the X-ray crystallographic analysis. A total of 665 frames were collected. The integration of the data using a triclinic unit cell yielded a total of 176 238 reflections to a maximum θ angle of 28.43° (0.75 Å resolution), of which 23 334 were independent (average redundancy 7.553, completeness = 99.3%, R_{int} = 6.22%, R_{sig} = 4.33%) and 17 730 (75.98%) were greater than 2$\sigma(F^2)$. The final cell constants of a = 11.8831(7) Å, b = 19.9377(11) Å, c = 20.9074(12) Å, α = 70.752(2)°, β = 85.908(2)°, γ = 88.956(2)°, volume = 4664.5(5) Å^3, are based upon the refinement of the XYZ-centroids of 9848 reflections above 20 $\sigma(I)$ with 5.559° < 2θ < 56.03°. The ratio of minimum to maximum apparent transmission was 0.908. The calculated minimum and maximum transmission coefficients (based on crystal size) are 0.8710 and 0.9320.

The structure was solved and refined using the space group $P\bar{1}$, with Z = 4 for the formula unit, C$_{42}$H$_{43}$Cl$_4$F$_6$N$_7$O$_5$P$_2$Ru. The final anisotropic full-matrix least-squares refinement on F^2 with 1294 variables converged at R_1 = 7.15%, for the observed data and wR_2 = 17.81% for all data. The goodness-of-fit was 1.136. The largest peak in the final difference electron density synthesis was 1.760 e$^-$ Å^{-3} and the largest hole was −1.669 e$^-$ Å^{-3} with an RMS deviation of 0.126 e$^-$ Å^{-3}. On the basis of the final model, the calculated density was 1.630 g cm^{-3} and $F(000)$, 2320e$^-$. The Fluorines of one of the PF6− anions was disordered and modelled with the PART command with occupancies close to 50% over two sites. One of the solvent CH2Cl2 molecules was disordered and modelled with the PART command with occupancies of 60% and 40% over two sites. The phenyl ring C30-C35 was disordered and modelled with the PART command with occupancies of 70% and 30% over two sites. The phenyl ring C24a-C29a was disordered and modelled with the PART command with occupancies of 60% and 40% over two sites. One of the CH2-Piperazine moiety, atoms c36A, N37A, C38A, C39A, N40A, C41A and C42A was disordered and modelled with the PART command with occupancies of 50% over two sites.

[Ru(η^5-C$_5$H$_5$)(phen)(Ph$_2$P-CH$_2$-pip-NBD)][PF$_6$] (5). A red, needle-like specimen of 4(C$_{40}$H$_{35}$N$_7$O$_3$PRu), 4(F$_6$P), H$_2$O, approximate dimensions 0.110 mm × 0.110 mm × 0.400 mm, was used for the X-ray crystallographic analysis. A total of 994 frames were collected. The integration of the data using a monoclinic unit cell yielded a total of 42 107 reflections to a

maximum θ angle of 27.55° (0.77 Å resolution), of which 8902 were independent (average redundancy 4.730, completeness = 99.3%, R_{int} = 7.96%, R_{sig} = 6.28%) and 6595 (74.08%) were greater than 2$\sigma(F^2)$. The final cell constants of a = 18.1160(10) Å, b = 13.1312(8) Å, c = 16.5005(11) Å, β = 98.267(2)°, volume = 3884.4(4) Å^3, are based upon the refinement of the XYZ-centroids of 9918 reflections above 20 $\sigma(I)$ with 5.176° < 2θ < 54.68°. The ratio of minimum to maximum apparent transmission was 0.744. The calculated minimum and maximum transmission coefficients (based on crystal size) are 0.8050 and 0.9400.

The structure was solved and refined using the space group $P1$ $21/c1$, with Z = 1 for the formula unit, C$_{160}$H$_{142}$F$_{24}$N$_{28}$O$_{13}$P$_8$Ru$_4$. The final anisotropic full-matrix least-squares refinement on F^2 with 539 variables converged at R_1 = 4.81%, for the observed data and wR_2 = 9.10% for all data. The goodness-of-fit was 1.077. The largest peak in the final difference electron density synthesis was 0.75 e$^-$ Å^{-3} and the largest hole was −0.850 e$^-$ Å^{-3} with an RMS deviation of 0.103 e$^-$ Å^{-3}. On the basis of the final model, the calculated density was 1.613 g cm^{-3} and $F(000)$, 1914e$^-$.

Cell lines

In vitro studies were conducted in CT26 (murine colon cancer), 4T1 (murine triple negative breast cancer) and U2OS (human osteosarcoma), as well as in a murine fibroblast cell line, 3T3. The cells were purchased from ATCC (CRL-2638™, CRL-2539™, and CRL-1658™) whereas U2OS were provided by the Laboratory of Prof. Guido Kroemer. Cells were cultured in Dulbecco's Modified Eagle's medium (DMEM, Sigma) supplemented with 10% (v/v) heat-inactivated fetal bovine serum and 1% of a mixture penicillin/streptomycin and maintained in 75 cm^2 flasks at 37 °C in humidified atmosphere with 5% CO$_2$.

Viability assays

4T1, CT26 (5 × 10^3 per well), U2OS-WT (6 × 10^3 per well) and 3T3 (3 × 10^3 per well) cells were seeded in 96-well plates. After 24 hours, cells were treated with cisplatin, Ph$_2$P-CH$_2$-pip-NBD, and complexes **1–5**, at concentrations ranging from 0.78 to 100 μM, for 48 h. Cell viability was evaluated using the Alamar blue assay, which contains resazurin, a non-fluorescent blue dye that is metabolized by cells into resorufin, a pink and highly fluorescent compound. Then, the fluorescence of untreated cells (ctrl) was assumed to correspond to 100% of viability. Fluorescence was measured using a Synergy HT Multi-Mode Microplate Reader (BioTek) with excitation using a 528/20 nm filter and emission collected using a 590/35 nm filter.

Fluorescence quantum yield

The fluorescence quantum yield (Φ_F) was determined using a relative method, as described in the literature.[45] Solutions of the ruthenium compounds, as along with Rose Bengal as a reference compound with a known fluorescence quantum yield,[46] were prepared in dimethylsulfoxide at concentrations

ensuring absorbance values below 0.1 at 345 nm. Complexes **1–5**, Ph$_2$P-CH$_2$-pip-NBD, and Rose Bengal, were excited at λ = 345 nm, and their emission spectra were recorded over the 480–750 nm range using a Horiba-Jovin-Yvon Spex Fluorog 3–2.2 spectrophotometer. The fluorescence intensities were obtained by integrating the area under the emission curves, and the fluorescence quantum yields were calculated as described in.[45]

Cell uptake

4T1, 3T3 (4 × 10^4 per well), CT26 and U2OS (5 × 10^4 per well) cells were seeded in 24-well plates and let to adapt for 24 hours. Afterwards, cells were incubated with complexes **1–5** (6.25 and 12.5 μM) for 25 h at 37 °C. In parallel experiments, the impact of endocytosis inhibition in the internalization of the ruthenium compounds was also evaluated. For this, an additional step of pre-incubation of 30 minutes with an inhibitor of caveolin-mediated endocytosis (Genistein at 200 μM), or with an inhibitor of clathrin-mediated endocytosis (Chloroquine at 100 μM), was performed. Afterwards, complexes **1–5** and Ph$_2$P-CH$_2$-pip-NBD, were added to the cells, for an incubation of 6–7 hours.

In both protocols, at the indicated time points, cells were washed once with PBS, detached with trypsin-EDTA and centrifuged for 5 minutes at 2000 rpm. Cells were then resuspended in PBS and immediately analysed by flow cytometry (Agilent, Novocyte® 3000). The fluorescence associated to the Ru(II) compounds was measured upon excitation with the 488 nm laser, and detection was performed using the 530/30 nm filter. An average of 15 000 events were collected, and the data are presented as the mean fluorescence normalized to the mean fluorescence of untreated cells.

Intracellular localization evaluated by confocal microscopy

4T1 cancer cells (10 000 cells per well) were seeded in an 8-well iBidi plate. After 24 hours, complexes **1–5**, and Ph$_2$P-CH$_2$-pip-NBD, were added to the cells at concentrations of 9 μM, followed by an incubation period of 6 hours. Afterwards, 150 nM Lysotracker Red (Life Technologies) was added to the cells and let for 2.5 hours. Cells were then washed twice with PBS and images were acquired.

In a parallel experiment, cells were incubated for 30 minutes with chloroquine (100 μM) or genistein (200 μM), followed by the addition of complexes **1**, **3**, and **4** at a final concentration of 9 μM.

In both experiments, imaging was performed using a Carl Zeiss LSM 980 confocal microscope with excitation lasers set to 488 and 561 nm for complexes **1–5** and Lysotracker Red, respectively.

Partition coefficients of compounds between the aqueous phase and POPC:POPS bilayers

A lipid film of 1-Palmitoyl-2-oleoyl-*sn*-glycero-3-phosphocholine (POPC) and 1-Palmitoyl-2-oleoyl-sn-*glycero*-3-phospho-L-serine (POPS) was prepared by evaporating a mixture of POPC and POPS, at a molar ratio of 9:1, dissolved in an azeotropic

chloroform/methanol solution (87:13 v/v), with previous equilibration of the mixture for 30 minutes at room temperature. Large multilamellar vesicles (MLVs) were prepared by hydration of the lipid film with PBS (10 mM sodium phosphate at pH = 7.4 with 150 mM NaCl) to a total lipid concentration of 10 mM, followed by 3 cycles of freeze/taw (in liquid nitrogen and at 30 °C, respectively). For the preparation of large unilamelar vesicles (LUVs), the MLVs were first subject to 3 cycles of extrusion through two-staked polycarbonate 100 nm pore-size filters (Nucleopore) using a water-jacketed extruder (Lipex Biomembranes, Vancouver, British Columbia, Canada) with freeze/taw between the extrusions, followed by 10 additional extrusion steps.[47] The size and surface potential of the LUVs was characterized by dynamic light scattering and zeta potential measurements (Zetasizer Nano ZS, Malvern, UK).

The partition coefficients of the compounds were characterized by addition of the compounds dissolved in dimethyl-sulfoxide to LUVs solutions pre-warmed at 37 °C and 10 different lipid concentrations, with a final concentration of the compounds of 5 or 15 μM and 1% DMSO. The solutions were allowed to equilibrate for 5 minutes at 37 °C, and their fluorescence at λ_{exc} = 440 nm/λ_{em} = 590 nm was measured using a plate reader (SpectraMax iD5, Molecular Devices, Berkshire, UK). Blank LUVs solutions containing 1% DMSO were also prepared and the signal subtracted from that of the test solutions. Titrations with a maximum lipid concentration of 5 mM were performed with 100 μL solution in 96 well black/clear bottom plates (ThermoFisher Scientific Inc., Waltham, MA, USA), while for a maximum lipid concentration of 10 mM a spectra-drop micro-volume microplate with a light path of 0.5 mm (Molecular Devices, Berkshire, UK) was used to decrease possible artifacts due to high light scattering from the LUVs. The partition coefficient (K_P) was obtained from the best fit of eqn (1) for the variation of the fluorescence intensity (I) with the lipid concentration ([L]), which assumes simple partition, additivity in the fluorescence from the compound in the aqueous phase (I_W) and associated with the LUVs (I_M), and considering a molar lipid volume ($\overline{V}_L$) equal to 0.76 dm^3 mol^{-1}.[48]

$$I = \frac{I_W + I_M K_P \overline{V}_L [L]}{1 + K_P \overline{V}_L [L]} \tag{1}$$

Detection of ROS with CellROX™ ROS reagent

4T1 cells (50 000 cells per well) were seeded in 24-well plates. After 24 hours, compounds **1**, **3**, and **5** (15 and 25 μM) were added to the cells and incubated for 6 hours. Then, cells were stained with 5 μM of CellROX® Deep Red reagent (Thermo Fisher Scientific, Inc.) for 30 minutes, washed three times with PBS, detached using trypsin–EDTA, and centrifuged for 5 minutes at 2000 rpm. Afterwards, the cells were resuspended in PBS and immediately analyzed by flow cytometry (Agilent, NovoCyte® 3000). The fluorescence associated with the CellROX® red reagent was measured upon excitation with the

640 nm laser, and detection was performed using the 675/30 nm filter. An average of 12 000 events were collected, and the data are presented as the mean fluorescence normalized to the mean fluorescence of untreated cells.

Morphological changes evaluated by microscopy

4T1 cancer cells (20 000 cells per well) were seeded in 24-well plates. After 24 hours, compounds **1**, **3**, and **5** (15 and 25 μM) were added to the cells. Morphological changes were analyzed after 6, 24, and 48 hours of incubation using optical and fluorescence microscopy. For this, 1 μL of Hoechst 33342 (10 mg mL^{-1}, Thermo Fisher Scientific) was added to each well 20 minutes prior to imaging. Subsequently, cell images were immediately acquired using a ZEISS Axiovert 5 microscope equipped with an HXP 120 V fluorescence system and a 20× objective.

Conflicts of interest

There are no conflicts of interest.

Data availability

The data supporting this article have been included as part of the supplementary information (SI). Supplementary information is available. See DOI: https://doi.org/10.1039/d5dt01975c.

CCDC 2476799 (**1**), 2476798 (**3**) and 2476797 (**5**) contain the supplementary crystallographic data for this paper.[49a–c]

Acknowledgements

References

1 F. Bray, M. Laversanne, H. Sung, J. Ferlay, R. L. Siegel, I. Soerjomataram and A. Jemal, Global cancer statistics 2022: GLOBOCAN estimates of incidence and mortality worldwide for 36 cancers in 185 countries, *CA-Cancer J. Clin.*, 2024, **74**, 229–263, DOI: 10.3322/caac.21834.

2 R. L. Siegel, K. D. Miller, H. E. Fuchs, A. Jemal and F. Bray, Global cancer statistics 2020: GLOBOCAN estimates of incidence and mortality worldwide for 36 cancers in 185 countries, *CA-Cancer J. Clin.*, 2021, **71**, 209–249, DOI: 10.3322/caac.21590.

3 P. J. Dyson and G. Sava, Metal-based antitumour drugs in the post genomic era, *Dalton Trans.*, 2006, 1929–1933, DOI: 10.1039/b601840h.

4 S. Abdolmaleki, A. Aliabadi and S. Khaksar, Riding the metal wave: A review of the latest developments in metal-based anticancer agents, *Coord. Chem. Rev.*, 2024, **501**, 215579, DOI: 10.1016/j.ccr.2023.215579.

5 M. J. Piccart, H. Lamb and J. B. Vermorken, Current and future potential roles of the platinum drugs in the treatment of ovarian cancer, *Ann. Oncol.*, 2001, **12**, 1195–1203, DOI: 10.1023/A:1012259625746.

6 R. Oun, Y. E. Moussa and N. J. Wheate, The side effects of platinum-based chemotherapy drugs: a review for chemists, *Dalton Trans.*, 2018, **47**, 6645–6653, DOI: 10.1039/C8DT00838H.

7 S. Y. Lee, C. Y. Kim and T. Nam, Ruthenium Complexes as Anticancer Agents: A Brief History and Perspectives, *Drug Des., Dev. Ther.*, 2020, **14**, 5375–5392, DOI: 10.2147/DDDT.S275007.

8 A. Bergamo and G. Sava, Ruthenium anticancer compounds: myths and realities of the emerging metal-based drugs, *Dalton Trans.*, 2011, **40**, 7817–7823, DOI: 10.1039/C0DT01816C.

9 G. Gasser, I. Ott and N. Metzler-Nolte, Organometallic anticancer compounds, *J. Med. Chem.*, 2011, **54**, 3–25, DOI: 10.1021/jm100020w.

10 C. S. Allardyce and P. J. Dyson, Ruthenium in medicine: current clinical uses and future prospects, *Platinum Met. Rev.*, 2001, **45**, 62–69. Available from: https://technology.matthey.com/article/45/2/62-69/.

11 S. Thota, D. A. Rodrigues, D. C. Crans and E. J. Barreiro, Ru (II) compounds: next-generation anticancer metallotherapeutics?, *J. Med. Chem.*, 2018, **61**, 5805–5821, DOI: 10.1021/acs.jmedchem.7b01689.

12 I. Kostova, Ruthenium complexes as anticancer agents, *Curr. Med. Chem.*, 2006, **13**, 1085–1107, DOI: 10.2174/092986706776360941.

13 C. Sonkar, S. Sarkarb and S. Mukhopadhyay, Ruthenium (II)–arene complexes as anti-metastatic agents, and related techniques, *RSC Med. Chem.*, 2022, **13**, 22–38, DOI: 10.1039/D1MD00220A.

14 A. H. Velders, A. Bergamo, E. Alessio, E. Zangrando, J. G. Haasnoot, C. Casarsa, M. Cocchietto, S. Zorzet and G. Sava, Synthesis and chemical-pharmacological characterization of the antimetastatic NAMI-A-type Ru(III) complexes (Hdmtp)[trans-RuCl₄(dmso-*S*)(dmtp)], (Na)[trans-RuCl₄(dmso-*S*)(dmtp)], and [*mer*-RuCl₃(H₂O)(dmso-*S*)(dmtp)] (dmtp = 5,7-dimethyl[1,2,4]triazolo[1,5-*a*]pyrimidine), *J. Med. Chem.*, 2004, **47**, 1110–1121, DOI: 10.1021/jm030984d.

15 A. K. Bytzek, G. Koellensperger, B. K. Keppler and C. G. Hartinger, Biodistribution of the novel anticancer

drug sodium *trans*-[tetrachloridobis(1*H*-indazole)ruthenate (III)] KP-1339/IT139 in nude BALB/c mice and implications on its mode of action, *J. Inorg. Biochem.*, 2016, **160**, 250–255, DOI: 10.1016/j.jinorgbio.2016.02.037.

16 C. G. Hartinger, S. Zorbas-Seifried, M. A. Jakupec, B. Kynast, H. Zorbas and B. K. Keppler, From bench to bedside – preclinical and early clinical development of the anticancer agent indazolium *trans*-[tetrachlorobis(1*H*-indazole)ruthenate(III)] (KP1019 or FFC14A), *J. Inorg. Biochem.*, 2006, **100**, 891–904, DOI: 10.1016/j.jinorgbio.2006.02.013.

17 S. Monro, K. L. Colón, H. Yin, J. Roque, P. Konda, S. Gujar, R. P. Thummel, L. Lilge, C. G. Cameron and S. A. McFarland, Transition metal complexes and photodynamic therapy from a tumor-centered approach: challenges, opportunities, and highlights from the development of TLD1433, *Chem. Rev.*, 2019, **119**(2), 797–828, DOI: 10.1021/acs.chemrev.8b00211.

18 G. Gasser, I. Ott and N. Metzler-Nolte, Organometallic anticancer compounds, *J. Med. Chem.*, 2011, **54**, 3–25, DOI: 10.1021/jm100020w.

19 G. Suss-Fink, Arene ruthenium complexes as anticancer agents, *Dalton Trans.*, 2010, **39**, 1673–1688, DOI: 10.1039/B916860P.

20 Y. K. Yan, M. Melchart, A. Habtemariam and P. J. Sadler, Organometallic chemistry, biology and medicine: ruthenium arene anticancer complexes, *Chem. Commun.*, 2005, 4764–4776, DOI: 10.1039/B508531B.

21 T. S. Morais, A. Valente, A. I. Tomaz, F. Marques and M. H. Garcia, Tracking antitumor metallodrugs: promising agents with the Ru(II)- and Fe(II)-cyclopentadienyl scaffolds, *Future Med. Chem.*, 2016, **8**, 527–544, DOI: 10.4155/fmc.16.7.

22 S. Wu, X. Wang, C. Zhu, Y. Song, J. Wang, Y. Lia and Z. Guo, Monofunctional platinum complexes containing a 4-nitrobenzo-2-oxa-1,3-diazole fluorophore: distribution in tumour cells, *Dalton Trans.*, 2011, **40**, 10376–10382, DOI: 10.1039/C1DT10555H.

23 D. C. J. Waalboer, J. A. Muns, N. J. Sijbrandi, R. B. M. Schasfoort, R. Haselberg, G. W. Somsen, H. Houthoff and G. A. M. S. van Dongen, Platinum(II) as Bifunctional Linker in Antibody–Drug Conjugate Formation: Coupling of a 4-Nitrobenzo-2-oxa-1,3-diazole Fluorophore to Trastuzumab as a Model, *ChemMedChem*, 2015, **10**(5), 797–803, DOI: 10.1002/cmdc.201402496.

24 R. F. M. Almeida, T. C. B. Santos, L. C. Silva, J. Suchodolski, A. Krasowska, K. Stokowa-Sołtys, M. Puchalska and R. Starosta, NBD derived diphenyl(aminomethyl)phosphane – A new fluorescent dye for imaging of low pH regions and lipid membranes in living cells, *Dyes Pigm.*, 2021, **184**, 108771, DOI: 10.1016/j.dyepig.2020.108771.

25 S. A. Milheiro, J. Gonçalves, R. M. R. M. Lopes, M. Madureira, L. Lobo, A. Lopes, F. Nogueira, D. Fontinha, M. Prudêncio, M. M. Piedade, S. N. Pinto, P. R. Florindo and R. Moreira, Half-Sandwich Cyclopentadienylruthenium (II) Complexes: A New Antimalarial Chemotype, *Inorg.*

Chem., 2020, **59**(17), 12722–12732, DOI: 10.1021/acs.inorgchem.0c01795.

26 F. Geisslinger, M. Müller, A. M. Vollmar and K. Bartel, Targeting Lysosomes in Cancer as Promising Strategy to Overcome Chemoresistance—A Mini Review, *Front. Oncol.*, 2020, **10**, 1156, DOI: 10.3389/fonc.2020.01156.

27 F. Wang, R. Gómez-Sintes and P. Boya, Lysosomal membrane permeabilization and cell death, *Traffic*, 2018, **19**(12), 918–931, DOI: 10.1111/tra.12613.

28 M. Mohanty, S. Das, P. D. Pattanayak, S. Lima, W. Kaminsky and R. Dinda, Ru(III)–Morpholine-Derived Thiosemicarbazone-Based Metallodrugs: Lysosome-Targeted Anticancer Agents, *ACS Appl. Bio Mater.*, 2025, **8**(2), 1210–1226, DOI: 10.1021/acsabm.4c01536.

29 X. He, J. Chen, L. Wei, M. Kandawa-Shultz, G. Shao and Y. Wang, Antitumor activity of iridium/ruthenium complexes containing Nitro-substituted quinoline ligands *in vivo* and *in vitro*, *Dyes Pigm.*, 2023, **213**, 111146, DOI: 10.1016/j.dyepig.2023.111146.

30 Z. Liu, J. Li, D. Kong, M. Tian, Y. Zhao, Z. Xu, W. Gao and Y. Zhou, Dual Functional Half-Sandwich Ru(II) Complexes: Lysosome-Targeting Probes and Anticancer Agents, *Eur. J. Inorg. Chem.*, 2019, **2019**(2), 287–294, DOI: 10.1002/ejic.201801339.

31 J. Li, L. Guo, Z. Tian, S. Zhang, Z. Xu, Y. Han, R. Li, Y. Li and Z. Liu, Half-Sandwich Iridium and Ruthenium Complexes: Effective Tracking in Cells and Anticancer Studies, *Inorg. Chem.*, 2018, **57**(21), 13552–13563, DOI: 10.1021/acs.inorgchem.8b02161.

32 Z. Tian, J. Li, S. Zhang, Z. Xu, Y. Yang, D. Kong, H. Zhang, X. Ge, J. Zhang and Z. Liu, Lysosome-Targeted Chemotherapeutics: Half-Sandwich Ruthenium(II) Complexes That Are Selectively Toxic to Cancer Cells, *Inorg. Chem.*, 2018, **57**(17), 10498–10502, DOI: 10.1021/acs.inorgchem.8b01944.

33 Z. Xu, J. Huang, D. Kong, Y. Yang, L. Guo, X. Jia, G. Zhong and Z. Liu, Potent half-sandwich Ru(II) N^N (aryl-BIAN) complexes: Lysosome-mediated apoptosis, *in vitro* and *in vivo* anticancer activities, *Eur. J. Med. Chem.*, 2020, **207**, 112763, DOI: 10.1016/j.ejmech.2020.112763.

34 L. Côrte-Real, B. Karas, P. Gírio, A. Moreno, F. Avecilla, F. Marques, B. T. Buckley, K. R. Cooper, C. Doherty, P. Falson, M. H. Garcia and A. Valente, Unprecedented inhibition of P-gp activity by a novel ruthenium-cyclopentadienyl compound bearing a bipyridine-biotin ligand, *Eur. J. Med. Chem.*, 2019, **163**, 853–863, DOI: 10.1016/j.ejmech.2018.12.022.

35 R. G. Teixeira, D. C. Belisario, X. Fontrodona, I. Romero, A. I. Tomaz, M. H. Garcia, C. Riganti and A. Valente, Unprecedented collateral sensitivity for cisplatin-resistant lung cancer cells presented by new ruthenium organometallic compounds, *Inorg. Chem. Front.*, 2021, **8**, 1983–1996, DOI: 10.1039/D0QI01344G.

36 R. G. Teixeira, I. C. Salaroglio, N. F. B. Oliveira, J. G. N. Sequeira, X. Fontrodona, I. Romero, M. Machuqueiro, A. I. Tomaz, M. H. Garcia, C. Riganti and

A. Valente, Fighting Multidrug Resistance with Ruthenium–Cyclopentadienyl Compounds: Unveiling the Mechanism of P-gp Inhibition, *J. Med. Chem.*, 2023, **66**(20), 14080–14094, DOI: 10.1021/acs.jmedchem.3c01120.

37 R. G. Teixeira, J. P. Mészáros, B. Matos, L. Côrte-Real, C. P. R. Xavier, X. Fontrodona, M. H. Garcia, I. Romero, G. Spengler, M. H. Vasconcelos, A. I. Tomaz, É. A. Enyedy and A. Valente, Novel family of [RuCp(N,N)(P)]$^+$ compounds with simultaneous anticancer and antibacterial activity: biological evaluation and solution chemistry studies, *Eur. J. Med. Chem.*, 2023, **262**, 115922, DOI: 10.1016/j.ejmech.2023.115922.

38 W. Zhong, J. S. Myers, F. Wang, K. Wang, J. Lucas, E. Rosfjord, J. Lucas, A. T. Hooper, S. Yang, L. A. Lemon, M. Guffroy, C. May, J. R. Bienkowska and P. A. Rejto, Comparison of the molecular and cellular phenotypes of common mouse syngeneic models with human tumors, *BMC Genomics*, 2020, **21**, 2, DOI: 10.1186/s12864-019-6344-3.

39 R. M. S. Santos, J. Samelo, A. C. Oliveira, M. M. Cordeiro, M. J. Mora, G. E. Granero, H. A. L. Ffilipe, L. M. S. Loura and M. J. Moreno, Interaction of the Antibiotic Rifampicin with Lipid Membranes, *Biomolecules*, 2025, **15**(3), 320, DOI: 10.3390/biom15030320.

40 M. Zhou, H. Yang, H. Li, L. Gu, Y. Zhou and M. Li, The effects of molecular weight and orientation on the membrane permeation and partitioning of polycyclic aromatic hydrocarbons: a computational study, *Phys. Chem. Chem. Phys.*, 2022, **24**, 2158–2166, DOI: 10.1039/D1CP04777A.

41 T. I. Rokitskaya, E. V. Aleksandrova, G. A. Korshunova, L. S. Khailova, V. N. Tashlitsky, V. B. Luzhkov and Y. N. Antonenko, Membrane Permeability of Modified Butyltriphenylphosphonium Cations, *J. Phys. Chem. B*, 2022, **126**(2), 412–422, DOI: 10.1021/acs.jpcb.1c08135.

42 J. Pitchaimani, M. R. C. Raja, S. Sujatha, S. K. Mahapatra, D. Moon, S. P. Anthony and V. Madhu, Arene ruthenium(II) complexes with chalcone, aminoantipyrine and aminopyri-

midine based ligands: synthesis, structure and preliminary evaluation of anti-leukemia activity, *RSC Adv.*, 2016, **6**, 90982–90992, DOI: 10.1039/C6RA18504E.

43 S. Pal, Pragti, A. Kumara and S. Mukhopadhyay, Exploring the effect of Ru(II) arene complexes on cytotoxicity upon co-ligand variation and loading on amine-functionalized silica nanoparticles, *Dalton Trans.*, 2025, **54**, 7449–7457, DOI: 10.1039/D4DT03536D.

44 I. C. Salaroglio, D. Stefanova, R. G. Teixeira, N. F. B. Oliveira, A. Ahmed, F. Fusi, V. Tzankova, Y. Yordanov, M. Machuqueiro, S. Saponara, A. Valente and C. Riganti, A novel combinatory treatment against a CDDP-resistant non-small cell lung cancer based on a Ruthenium (II)-cyclopentadienyl compound, *Pharmacol. Res.*, 2024, **208**, 107353, DOI: 10.1016/j.phrs.2024.107353.

45 K. Rurack and M. Spieles, Fluorescence quantum yields of a series of red and near-infrared dyes emitting at 600–1000 nm, *Anal. Chem.*, 2011, **83**(4), 1232–1242, DOI: 10.1021/ac101329h.

46 S. M. Linden and D. C. Neckers, Type I and type II sensitizers based on Rose Bengal onium salts, *Photochem. Photobiol.*, 1988, **47**(4), 543–550, DOI: 10.1111/j.1751-1097.1988.tb08842.x.

47 J. Samelo, M. J. Mora, G. E. Granero and M. J. Moreno, Partition of Amphiphilic Molecules to Lipid Bilayers by ITC: Low-Affinity Solutes, *ACS Omega*, 2017, **2**, 6863–6869, DOI: 10.1021/acsomega.7b01145.

48 A. I. Greenwood, S. Tristram-Nagle and J. F. Nagle, Partial molecular volumes of lipids and cholesterol, *Chem. Phys. Lipids*, 2006, **143**, 1–10, DOI: 10.1016/j.chemphyslip.2006.04.002.

49 (*a*) CCDC 2476799: Experimental Crystal Structure Determination, 2025, DOI: 10.5517/ccdc.csd.cc2p49rx; (*b*) CCDC 2476798: Experimental Crystal Structure Determination, 2025, DOI: 10.5517/ccdc.csd.cc2p49qw; (*c*) CCDC 2476797: Experimental Crystal Structure Determination, 2025, DOI: 10.5517/ccdc.csd.cc2p49pv.